Arc-continent collision and orocline formation: Closing of the Central American seaway

Camilo Montes,[1,2] G. Bayona,[3] A. Cardona,[1,4] D. M. Buchs,[5] C. A. Silva,[6] S. Morón,[7] N. Hoyos,[1] D. A. Ramírez,[1] C. A. Jaramillo,[1] and V. Valencia[8]

Received 27 October 2011; revised 28 February 2012; accepted 28 February 2012; published 18 April 2012.

[1] Closure of the Central American seaway was a local tectonic event with potentially global biotic and environmental repercussions. We report geochronological (six U/Pb LA-ICP-MS zircon ages) and geochemical (19 XRF and ICP-MS analyses) data from the Isthmus of Panama that allow definition of a distinctive succession of plateau sequences to subduction-related protoarc to arc volcaniclastic rocks intruded by Late Cretaceous to middle Eocene intermediate plutonic rocks (67.6 ± 1.4 Ma to 41.1 ± 0.7 Ma). Paleomagnetic analyses (24 sites, 192 cores) in this same belt reveal large counterclockwise vertical-axis rotations (70.9° ± 6.7°), and moderate clockwise rotations (between 40° ± 4.1° and 56.2° ± 11.1°) on either side of an east-west trending fault at the apex of the Isthmus (Rio Gatun Fault), consistent with Isthmus curvature. An Oligocene-Miocene arc crosscuts the older, deformed and segmented arc sequences, and shows no significant vertical-axis rotation or deformation. There are three main stages of deformation: 1) left-lateral, strike-slip offset of the arc (~100 km), and counterclockwise vertical-axis rotation of western arc segments between 38 and 28 Ma; 2) clockwise rotation of central arc segments between 28 and 25 Ma; and 3) orocline tightening after 25 Ma. When this reconstruction is placed in a global plate tectonic framework, and published exhumation data is added, the Central American seaway disappears at 15 Ma, suggesting that by the time of northern hemisphere glaciation, deep-water circulation had long been severed in Central America.

Citation: Montes, C., G. Bayona, A. Cardona, D. M. Buchs, C. A. Silva, S. Morón, N. Hoyos, D. A. Ramírez, C. A. Jaramillo, and V. Valencia (2012), Arc-continent collision and orocline formation: Closing of the Central American seaway, *J. Geophys. Res.*, *117*, B04105, doi:10.1029/2011JB008959.

1. Introduction

[2] Final closure of the Central American seaway, separating the waters of the Pacific Ocean from the Caribbean Sea in Pliocene times, has been considered as the trigger for northern hemisphere glaciations [*Burton et al.*, 1997; *Haug et al.*, 2001; *Lear et al.*, 2003], and major biotic events documented in land and marine faunas [*Marshall et al.*, 1982; *Jackson et al.*, 1993]. Full closure and separation of waters may have been achieved through gradual shoaling and emergence of a Central American barrier [*Whitmore and Stewart*, 1965; *Coates et al.*, 2004] somewhere between westernmost South America and the Panama Canal Basin [*Kirby and MacFadden*, 2005]. This barrier, represented today by the San Blas Range (Figure 1), contains no record of any significant Neogene volcanic activity. Its emergence above sea level, must therefore have been achieved by a non-magmatic process, one probably related to deformation following collision of the Central American arc with the South American continent.

[3] The intervening zone between the active Central American volcanic arc [*de Boer et al.*, 1988; *MacMillan et al.*, 2004] and the South American continent, is the curvilinear Isthmus of Panama, where three tectonic segments (numbered 1 to 3 in Figure 1) can be defined from west to east: 1) the eastern tip of the subduction-related active Central American volcanic arc, with El Valle volcano as its easternmost stratovolcano (from 5 to 10 Ma to 0.1 Ma [*Defant et al.*, 1991a; *Hidalgo et al.*, 2011]); 2) a curved segment (the San Blas Range), paired with a submarine deformation belt to the north [*Silver et al.*, 1990, 1995], where incipient underthrusting of the Caribbean Plate may

[1]Smithsonian Tropical Research Institute, Balboa, Panama.
[2]Geociencias, Universidad de los Andes, Bogotá, Colombia.
[3]Corporacion Geologica Ares, Bogota, Colombia.
[4]Ingenieria de Petroleos, Universidad Nacional de Colombia, Medellín, Colombia.
[5]Research Division 4: Dynamics of the Ocean Floor, GEOMAR, Helmholtz Centre for Ocean Research Kiel, Kiel, Germany.
[6]Department of Geology, Oklahoma State University, Stillwater, Oklahoma, USA.
[7]Department of Geology, University of Minnesota, Minneapolis, Minnesota, USA.
[8]Department of Earth and Environmental Sciences, Washington State University, Pullman, Washington, USA.

0148-0227/12/2011JB008959

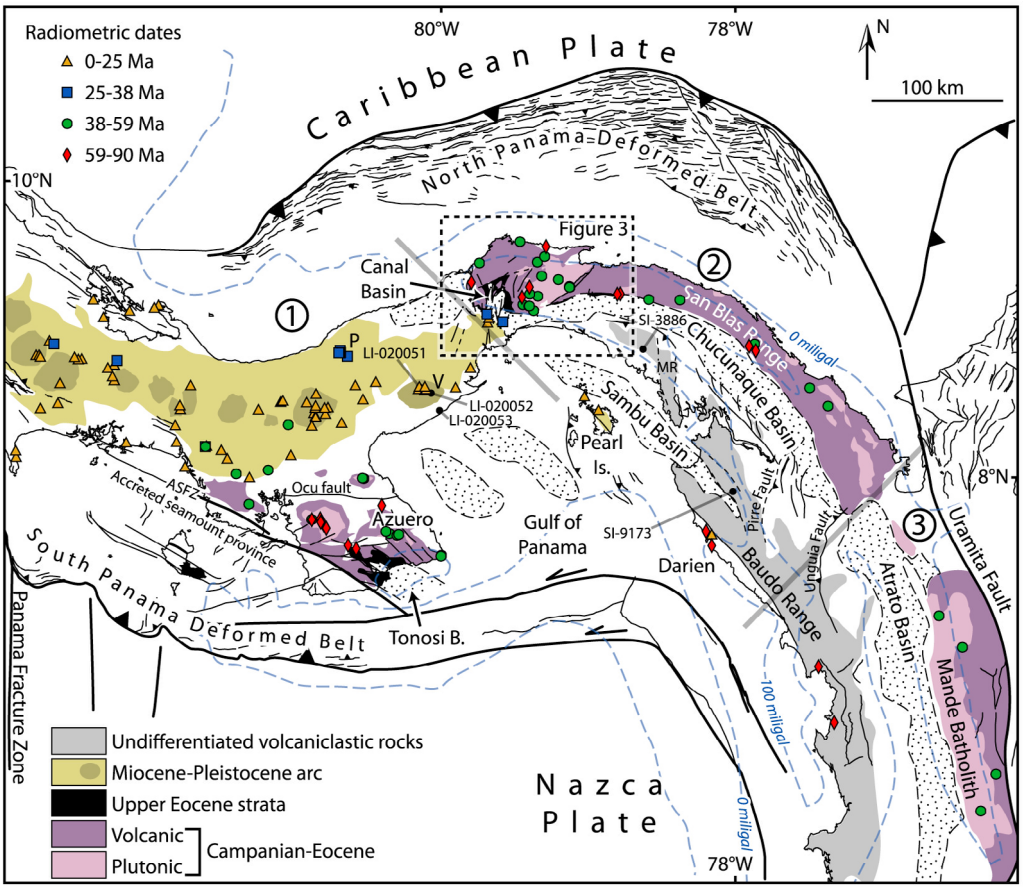

Figure 1. Tectonic setting of the Isthmus of Panama. Three segments (numbered 1 to 3) can be recognized on the basis of spatial distribution of lithologic types and radiometric ages: segment 1: Chorotega Block; segment 2: Panama Block; segment 3: Choco Block (maps compiled from *Woodring* [1957], *Recchi and Metti* [1975], *Lowrie et al.* [1982], *Duque-Caro* [1990a], *Mann and Corrigan* [1990], *Silver et al.* [1990], *Westbrook* [1990], *Defant et al.* [1991a], *Kolarsky and Mann* [1995], *Mann and Kolarsky* [1995], *Moore and Sender* [1995], *Kerr et al.* [1997b], *Coates et al.* [2004], *Morell et al.* [2008], *Buchs et al.* [2010], and *Montes et al.* [2012]; geochronologic data compiled from *Guidice and Recchi* [1969], *Kesler et al.* [1977], *Sillitoe et al.* [1982], *Aspden et al.* [1987], *Defant et al.* [1991a, 1991b], *Maury et al.* [1995], *Speidel et al.* [2001], *Lissina* [2005], *Rooney et al.* [2011], *Wegner et al.* [2011], and *Montes et al.* [2012]). ASFZ: Azuero-Sona Fault zone, MR: Maje Range, P: Petaquilla, V: El Valle Volcano.

be taking place [*Camacho et al.*, 2010]; and 3) a north-south trending segment accreted to the South American continental margin along the Uramita fault [*Duque-Caro*, 1990a]. Deformation leading to final closure of the Central American seaway must be recorded in these three segments, where subduction-related processes have generated magmatic products that can be used to trace the history of deformation.

[4] Here we refine a regional-scale strain marker originally defined by *Recchi and Metti* [1975], that we use to reconstruct the geometry of the Isthmus from middle Eocene times. We use the geochemistry of basaltic sequences, and the U/Pb crystallization ages of intermediate plutonic rocks to test the homogeneity of magmatic products from the Azuero Peninsula to the San Blas Range (Figure 1). These products define a uniform sequence composed of: 1) basaltic sequences with a distinctive progression of geochemical signatures from oceanic plateau to supra-subduction arc; 2) Late Cretaceous to middle Eocene intermediate plutonic rocks intruding the aforementioned basaltic sequences; and 3) upper Eocene to Oligocene, sub-aerial to shallow marine strata unconformably covering both basaltic and intermediate plutonic rocks. We call this coherent sequence the Campanian to Eocene belt, already recognized from southern Costa Rica to central Panama [*Buchs et al.*, 2010; *Wegner et al.*, 2011], and now recognized in eastern Panama to western Colombia. We use this coherent sequence as a strain marker where paleomagnetic declination data constrain maximum vertical-axis rotation of blocks. A younger volcanic belt, crosscutting the Campanian to Eocene belt is continuous, effectively dating the age of segmentation and deformation of this belt. Once the reconstruction here developed is placed in paleogeographic space, the gap between southern Central America and South America narrows well-before late Pliocene times, challenging the widely held idea that late

Pliocene closure of the Central American seaway changed the Earth's climate.

2. Regional Geological Setting

[5] Despite the paucity of field data in the Isthmus of Panama, regional kinematic reconstructions provide important clues regarding the space available for a seaway between the Americas during Cenozoic times. Using this approach, seminal papers by *Pindell and Dewey* [1982], and *Wadge and Burke* [1983] depicted collision between southernmost Central America and northwestern South America after 10 Ma. Later, *Pindell* [1993] reviewed the tectonic model and proposed a scenario where a migrating triple junction caused a deepwater, South American fore-arc basin (Pinon Basin), to be uplifted in response to Panama Ridge passing by in Paleocene-early Eocene times. The triple junction is generated as soon as the Costa Rica Panama and Choco supra-subduction arc is established in Campanian times. In this model, the Panama-South American blocks start head-on motion in middle Eocene times, and collide in early Oligocene times as marked by the termination of magmatism in the Panama-Choco block. This model is further revised [*Pindell et al.*, 2005] by proposing that this early Oligocene collision drives the formation of the North Panama Deformed Belt. *Pindell and Kennan* [2009] further review the chronology with the triple junction migration starting in latest Cretaceous times (71 Ma), the southern part of Panama accreting into the Ecuadorian fore-arc at 46 Ma the, and the North Panama Deformed Belt forming at 19 Ma.

3. The Panama-Choco Block

[6] The Chorotega, Panama and Choco blocks (numbered 1 to 3 in Figure 1) are located at the complex junction between Nazca, Cocos, Caribbean and South American plates [*Molnar and Sykes*, 1969]. These blocks are composed entirely of Cenozoic and Mesozoic magmatic products related to subduction, plateau volcanism and ocean island accretion [*de Boer et al.*, 1991; *Defant et al.*, 1991a, 1991b; *de Boer et al.*, 1995; *Maury et al.*, 1995; *Buchs et al.*, 2010, 2011a; *Wegner et al.*, 2011], as well as sedimentary basins that developed on these magmatic products [*Stewart et al.*, 1980; *Kolarsky et al.*, 1995; *Coates and Obando*, 1996]. Several phases of volcanic activity have been defined by along-strike and temporal changes in the position of the volcanic front and composition of the igneous rocks along the Isthmus of Panama [*de Boer et al.*, 1995; *Lissina*, 2005; *Gazel et al.*, 2011; *Wegner et al.*, 2011]. A Late Campanian (~75–73 Ma) arc initiation is documented in southern Costa Rica and western Panama by protoarc igneous rocks emplaced within and on top of an oceanic plateau (~89–85 Ma) found at the base of mature arc sequences [*Buchs et al.*, 2010, and references therein]. This oceanic plateau is likely to be part of the Caribbean Large Igneous Province, which covers most of the Caribbean Plate and may constitute a similar arc basement in most of the Isthmus [*Kerr et al.*, 1997a; *Lissina*, 2005; *Buchs et al.*, 2010]. However, plateau and protoarc sequences have yet to be identified east of the Panama Canal Basin. Younger magmatic products define the active Central American volcanic arc, a Miocene and younger arc [*Coates and Obando*, 1996; *MacMillan et al.*, 2004; *Lissina*, 2005] continuous from Guatemala to western Panama, where the El Valle Volcano represents its easternmost active strato-volcano [*Defant et al.*, 1991a; *Hidalgo et al.*, 2011].

[7] The Chorotega and Panama-Choco blocks record a long history of internal deformation [*Lowrie et al.*, 1982; *Mann and Corrigan*, 1990], both Paleogene [*Corral et al.*, 2011; *Farris et al.*, 2011; *Montes et al.*, 2012], and Neogene to recent in age [*Pratt et al.*, 2003; *Rockwell et al.*, 2010a, 2010b]. Bending of the Isthmus is thought to have been produced by Neogene northwest-trending, left-lateral strike-slip faulting, and subduction (remote sensing [*Mann and Corrigan*, 1990]), or by pure oroclinal bending (side scan and seismic data [*Silver et al.*, 1990]). GPS studies have shown that the Panama-Choco block continues to be translated relative to the Caribbean and South American plates [*Kellogg and Vega*, 1995; *Trenkamp et al.*, 2002]. Field and analytical studies in the Panama-Choco blocks show that the plutonic roots were exhumed from ~200°C to less than 60°C in the 47 to 42 Ma interval [*Villagomez*, 2010; *Montes et al.*, 2012], followed by a temporary cessation of magmatism between 38 and 28 Ma east of the Panama Canal Basin. North-verging folding, left-lateral strike-slip faulting [*Montes et al.*, 2012], and post-orogenic, partially terrestrial sedimentation (e.g., Gatuncillo and Tonosi formations [*Woodring*, 1957; *Kolarsky et al.*, 1995; *Lissina*, 2005; *Montes et al.*, 2012]) are related to this deformation event.

3.1. Boundaries of the Panama-Choco Block

[8] The northern boundary of the Isthmus of Panama (Figure 1) is a submarine, westward-tapering deformed belt [*Silver et al.*, 1990, 1995], where fault plane solutions of earthquakes mechanisms show shortening and incipient southward subduction/underthrusting of the Caribbean plate beneath the Isthmus [*Wolters*, 1986; *Adamek et al.*, 1988; *Camacho et al.*, 2010]. The age of formation of this belt is poorly known, but assuming a constant rate of convergence between the Caribbean Plate and the Isthmus of Panama (~10 km/Ma [*Kellogg and Vega*, 1995]), and factoring the ~150 km penetration of the Caribbean plate underneath the Isthmus south of the toe of the deformation belt [*Camacho et al.*, 2010], a middle Miocene age of initiation may be inferred.

[9] To the south, the boundary has been interpreted as a left-lateral transform separating the shallow Panama Gulf platform from the Nazca Plate [*Jordan*, 1975; *Kellogg and Vega*, 1995; *Westbrook et al.*, 1995], and as normal subduction west of the Azuero Peninsula [*Moore and Sender*, 1995]. An allochthonous belt of oceanic material is present in the fore-arc from Costa Rica to western Panama (Figure 1), south of the Azuero-Sona fault zone (Figure 1) where accretionary complexes and accreted seamounts were emplaced along the Middle American margin between the Late Cretaceous and Miocene [*Di Marco et al.*, 1995; *Hauff et al.*, 2000; *Hoernle et al.*, 2002, 2004; *Lissina*, 2005; *Baumgartner et al.*, 2008; *Hoernle et al.*, 2008; *Buchs et al.*, 2009, 2011a].

[10] To the east, similar Late Cretaceous ages and geochemical character of the volcanic basement [*Kerr et al.*, 1997b; *Lissina*, 2005], and similar basin configuration and age [*Case*, 1974; *Kellogg and Vega*, 1995; *Trenkamp et al.*, 2002; *Coates et al.*, 2004] indicate that the Atrato Basin is

the southeastern continuation of the Chucunaque Basin of the Panama-Choco Block. The Uramita Fault (Figure 1) therefore bounds the Panama-Choco Block to the east [*Duque-Caro*, 1990b; *Mann and Corrigan*, 1990; *Mann and Kolarsky*, 1995] with an uncertain deformational history [*Pindell and Kennan*, 2009]. Prior to suturing, the Uramita fault would have allowed the subduction of the Farallon/Nazca Plate under Central American and western South America while bringing the Central American arc closer to the continent [*Pindell and Dewey*, 1982; *Wadge and Burke*, 1983; *Kennan and Pindell*, 2009].

[11] A strike-slip structure [*Wolters*, 1986], sometimes called the Canal Fracture Zone with left-lateral [*de Boer et al.*, 1991] or right-lateral [*Lowrie et al.*, 1982] movement, is interpreted to separate the Chorotega from the Panama block. Even though gravity maps [*Case*, 1974] show the abrupt termination of a belt of positive anomalies all along the San Blas Range (Figure 1), detailed geologic mapping [*Woodring*, 1957; *Stewart et al.*, 1980] does not support the presence of such a fault in the immediate vicinity of the Panama Canal Basin, so if present, should be southwest of the Canal Basin. However, young volcanic products, mostly produced by the El Valle Volcano (Figure 1) in the last 10 Ma [*Defant et al.*, 1991a; *Hidalgo et al.*, 2011], conceal the geology southwest of the Canal Basin, except for the northernmost part, north of the Rio Gatun Fault.

4. Methodology

4.1. U/Pb Geochronology

[12] U-Pb-Th geochronology was conducted at the University of Arizona following procedures described by *Valencia et al.* [2005] and *Gehrels et al.* [2006, 2008]. Zircon crystals were recovered from granitoid samples by crushing and grinding, followed by separation with a Wilfley table, heavy liquids, and a Frantz magnetic separator. Samples were processed such that all zircons were retained in the final heavy mineral fraction. Zircons were incorporated into a 1″ epoxy mount together with fragments of Sri Lanka standard zircon. The mounts were sanded down to a depth of ~20 microns, polished, and cleaned prior to isotopic analysis.

[13] Zircon crystals were analyzed in a Micromass Isoprobe multicollector inductively coupled plasma mass spectrometer (ICP-MS) equipped with nine Faraday collectors, an axial Daly collector, and four ion-counting channels. Most of the analyses were done at the zircon tips in order to constrain the late zircon crystallization history [*Valencia et al.*, 2005]. Cathodoluminescence images on selected samples were obtained after U-Pb analysis at the Center for Electron Microscopy and Microanalysis of the University of Idaho in order to review the analytical premise of single growth zircon histories at the tips.

[14] U-Pb zircon crystallization ages (weighted averages) were estimated and plot using Isoplot 3.62 [*Ludwig*, 2007] and Arizona LaserChron Excel macro age pick program. Reported ages are 206Pb/238U, as they are Cenozoic samples. The uncertainty of the age is determined as the quadratic sum of the weighted mean error plus the total systematic error for the set of analyses. The systematic error, which includes contributions from the standard calibration, age of the calibration standard, composition of common Pb, and U decay constants, is generally ~1–2% (2-sigma).

4.2. Geochemistry

[15] Samples were reduced to powder using a pre-contaminated agate mill and analyzed at the Australian National University. Major elements SiO2, TiO2, Al2O3, Fe2O3, MnO, MgO, CaO, Na2O, K2O, P2O5, SO3, F and Cl were assessed by XRF with a Phillips (PANalytical) PW2400 X-ray fluorescence spectrometer at the Research School of Earth Sciences of RSES, The Australian National University (Tables 3a and 3b). Lithium tetraborate discs were prepared by fusion of 0.2700 g of dried sample powder and 1.7200 g of "12–22" eutectic lithium metaborate-lithium tetraborate. The major elements were calibrated against 28 international standard rock powders. LOI (loss on ignition) was obtained by heating sample powders at 1050°C during 1 h. Trace elements (i.e., Sc, Ti, V, Cr, Mn, Ni, Cu, Zn, Ga, Rb, Sr, Y, Zr, Nb, Ba, La, Ce, Pr, Nd, Sm, Eu, Gd, Tb, Dy, Ho, Er, Tm, Yb, Lu, Hf, Ta, Pb, Th, and U) were measured by laser ablation-ICP-MS on tetraborate glasses at the RSES. Glass disk used for ICP-MS analyses were prepared by fusion of 0.5000 g dried sample powder and 1.5000 g of "12–22" eutectic lithium metaborate-lithium tetraborate. A pulsed 193 nm ArF Excimer laser, with 50 mJ energy at a repetition rate of 5 Hz, coupled to an Agilent 7500S quadrupole ICP-MS were used. A synthetic glass (NIST 612) was used as standard material. Si values obtained from XRF analysis were used as internal standard. All chemical compositions used in this study were recalculated on an anhydrous basis before we interpreted them. Large volcanic intrusives, submarine volcanism and tropical weathering are factors of widespread alteration in the studied area. Alteration of igneous rocks is indicated by occurrence of secondary epidote, chlorite, pyrite, calcite and zeolites, significant LOI variations (i.e., 0.71 to 11.75 wt%), and anomalously high sulphur contents (SO3 > 1 wt%) in some samples (Tables 3a and 3b). Therefore, our interpretations are mostly based on elements known to be immobile during alteration processes (e.g., Th, Nb, Ta, rare earth elements, Ti).

4.3. Paleomagnetism

[16] Oriented cores for paleomagnetic analyses (Table 1) were collected using a portable drill and cut to the standard 2.4 cm diameter by 2.2 cm long in the laboratory. At least six cores were taken at each site, and sites were separated stratigraphically and structurally allowing tilt and unconformity tests to be made. Demagnetization processes were carried out at the Research Center for Paleomagnetism and Environmental Magnetism of the University of Florida (Gainesville, FL), using a 2G 755R cryogenic magnetometer, an ASC TD-48 thermal demagnetizer, a D Tech 2000 AF demagnetizer and a Bartington MS2 magnetic susceptibility meter. To decide on the best demagnetization technique for each site, we demagnetized two pilot samples per site, one thermally and the other with alternating fields. Demagnetization steps for alternate fields were from 5 to 50 mT at 5 mT steps and from 50 to 100 mT at 10 mT steps. Thermal demagnetization steps in degrees Celsius as follows: 100, 200, 300, 400, 450, 500, 540, 580, 600, 620, 640 and 660. We analyzed the paleomagnetic data using the IAPD 2000 software [*Torsvik et al.*, 2000]. Components of magnetization

Table 1. Overall Coordinate Samples and Names

Sample/ Locality	Location		Lithology
	Long (°W)	Lat (°N)	
		Geochemistry	
SI-2685	79°05′49,44″	9°14′25,79″	Basalt pillow
SI-2688	79°06′19,60″	9°14′27,96″	Basalt pillow
SI-2690	79°06′31,50″	9°14′18,90″	Basalt pillow
SI-2693	79°06′47,88″	9°14′31,35″	Basalt amigdular/vesicular
SI-3793	79°05′57,53″	9°14′32,80″	Basalt
SI-3754	78°58′46,64″	9°16′43,73″	Basalt
SI-3756	79°15′20,05″	9°10′05,52″	Basalt
SI-3758	79°15′26,11″	9°10′05,37″	Basalt dike
SI-3796	78°57′27,92″	9°15′40,46″	Porphytic basalt
SI-3797	78°57′27,91″	9°15′40,46″	Basalt dike
SI-3801	78°58′28,55″	9°14′39,22″	Basalt amigdular/vesicular dike
SI-3802	78°58′28,68″	9°14′39,24″	Pillow basalt
SI-3805	78°58′39,05″	9°14′23,14″	Basalt dike
SI-3764	79°20′36,28″	9°09′59,84″	Basalt dike
SI-9173	78°02′16,17″	7°54′17,91″	Basalt
SI-2655	79°15′15,13″	9°13′50,20″	Basalt dike
SI-2658	79°15′08,46″	9°10′37,29″	Basalt
SI-2664	79°15′17,12″	9°10′04,29″	Basalt dike
SI-3886	78°37′56,71″	8°51′28,15″	Basalt
		Paleomagnetism	
LI-010211	79°05′57,53″	9°14′32,80″	Diabase
LI-020004	79°39′14,24″	9°02′51,60″	Lithic tuff
LI-020017	79°39′12,70″	9°02′49,20″	Basaltic lava
LI-020019	79°38′47,52″	9°02′18,92″	Basaltic lava
LI-020048	79°45′44,80″	9°17′14,60″	Deep marine sed.
LI-020050	79°39′55,90″	9°15′20,40″	Tuffaceous ss
LI-020051	80°09′03,10″	8°36′54,00″	Andesitic lava
LI-020052	80°04′25,10″	8°34′28,30″	Volcanic breccia
LI-020053	80°00′42,60″	8°27′09,30″	Tuffaceous mud
LI-020088	79°45′46,73″	9°17′16,48″	Deep marine sed.
LI-020089	79°44′49,74″	9°17′21,91″	Deep marine sed.
LI-020092	79°38′18,16″	9°14′30,91″	Deep marine sed.
LI-020093	79°38′17,58″	9°14′30,30″	Basaltic lava
LI-020126	78°58′38,63″	9°14′23,00″	Calcareous sandstone
LI-020128	78°58′34,68″	9°14′07,68″	Lapilli tuff
LI-020130	78°58′34,68″	9°14′07,68″	Andesitic dike
LI-020132	79°05′57,98″	9°14′33,79″	Basalt
LI-020133	79°05′57,98″	9°14′33,79″	Basaltic dike
LI-020134	79°05′57,98″	9°14′33,79″	Diabase
LI-020143	79°06′41,98″	9°14′27,71″	Pillow basalt
LI-020144	79°06′58,36″	9°15′14,45″	Basalt
LI-040216	79°38′46,24″	9°02′21,42″	Lithic tuff
LI-020047	79°47′53,40″	9°19′14,50″	Basaltic lava
		Geochronology	
SI-924	80°31′30,90″	7°59′30,40″	Tonalite, 41.1 ± 0.7 Ma
SI-926	80°31′54,70″	7°59′33,40″	Tonalite, 48.1 ± 1.2 Ma
SI-1234	80°49′02,90″	7°43′09,50″	Granodiorite, 67.6 ± 1.4 Ma
SI-1237	80°48′54,80″	7°41′49,90″	Tonalite, 66.0 ± 1.0 Ma
SI-1238	80°47′39,80″	7°40′44,10″	Tonalite, 67.6 ± 1.0 Ma
SI-1248	80°22′27,90″	7°37′59,50″	Tonalite, 49.2 ± 0.9 Ma

were calculated by means of principal component analysis [*Kirschvink*, 1980] interpreted with the aid of orthogonal demagnetization diagrams of *Zijderveld* [1967]. Mean magnetization directions were calculated using Fisher's statistics [*Fisher*, 1953]. The incremental tilt test [*McFadden and Reid*, 1982] and the unconformity test were used to determine the timing of magnetization using the difference in direction between basement and cover sequences. The significance of the tilt test followed the criteria of *McElhinny* [1964] because of the limited number of sites per structural domain. For vertical-axis rotations, the confidence limits for structural domain declinations and the relative difference of declinations with the present declination in an arbitrary point in central Panama (9.25°N, 280.25°E) follow the criteria given by *Demarest* [1983].

5. Results

5.1. Geochronology

[17] Five samples of tonalites and one granodiorite were chosen for zircon separation and U/Pb age dating northeast of the Azuero-Sona fault zone (Figure 1). Zircon crystals from the six granitoid samples are characterized by width/length ratios of 1:2 to 1:3 with crystallization ages (Figure 2 and Table 2) ranging between Maastrichtian and Lutetian (67.6 ± 1 Ma, 67.6 ± 1.4 Ma, 66 ± 1.0 Ma, 49.2 ± 0.9 Ma, 48.1 ± 1.2 Ma, 41.1 ± 0.7 Ma). Internal cathodoluminescence patterns show single-pattern oscillatory zoning with no multiple growth patches, usually associated to older zircon crystals (Figure 2), so there is no inherited zircons linked to multiple-stage granitoids [*Hoskin and Schaltegger*, 2003; *Hawkesworth et al.*, 2004]. These features, along with U/Th ratios <12 (Table 2), are typical of igneous zircons [*Rubatto*, 2002; *Corfu et al.*, 2003]. These magmatic zircons were recovered from intermediate plutonic rocks that locally develop thermal contact aureolas within the Late Cretaceous volcanic-sedimentary sequence they intrude [*Buchs et al.*, 2010; *Corral et al.*, 2011].

[18] Existing ages in the intermediate plutonic suite of the Azuero Peninsula consist of one K/Ar age (69 ± 10 Ma) on a quartz-diorite with andesine, quartz, hornblende, and orthopyroxene in central Azuero [*Guidice and Recchi*, 1969], and two K/Ar samples in northwestern Azuero [*Kesler et al.*, 1977], with ages of 64.9 ± 1.3 Ma in hornblende, and 52.6 ± 0.6 Ma in feldspar of a quartz-diorite with quartz, plagioclase, hornblende, minor potassium feldspar, and magnetite. A similar quartz-diorite in southern Azuero, yielded 53 ± 3 Ma, also using K/Ar techniques [*Guidice and Recchi*, 1969]. *Lissina* [2005] reports three plagioclase Ar/Ar ages from granite and granodiorite (50.6 ± 0.3 Ma, 50.7 ± 0.1 Ma, and 49.5 ± 0.2 Ma) also in the same suite of intrusives of central Azuero. Our six new U/Pb radiometric crystallization ages in the Azuero Peninsula range between 67 and 41 Ma (Figure 2 and Table 2), complementing the existing geochronologic database (seven K/Ar and Ar/Ar determinations between 69 and 49 Ma) for the intermediate suite of plutonic rocks intruding basaltic sequences.

[19] In summary, new and existing geochronologic data in the Azuero Peninsula document the presence of an intermediate plutonic suite of Campanian to middle Eocene age that is similar in age and composition to a suite of intermediate plutonic rocks mapped in the San Blas Range [*Wegner et al.*, 2011; *Montes et al.*, 2012]. This intermediate plutonic suite intrudes a volcaniclastic succession in the San Blas Range and in the Azuero Peninsula. In the next section we present the geochemistry data for the basaltic sequence in the San Blas Range.

5.2. Geochemistry

[20] While the basaltic sequences in the Azuero Peninsula are well known and studied [*Buchs et al.*, 2010, and references

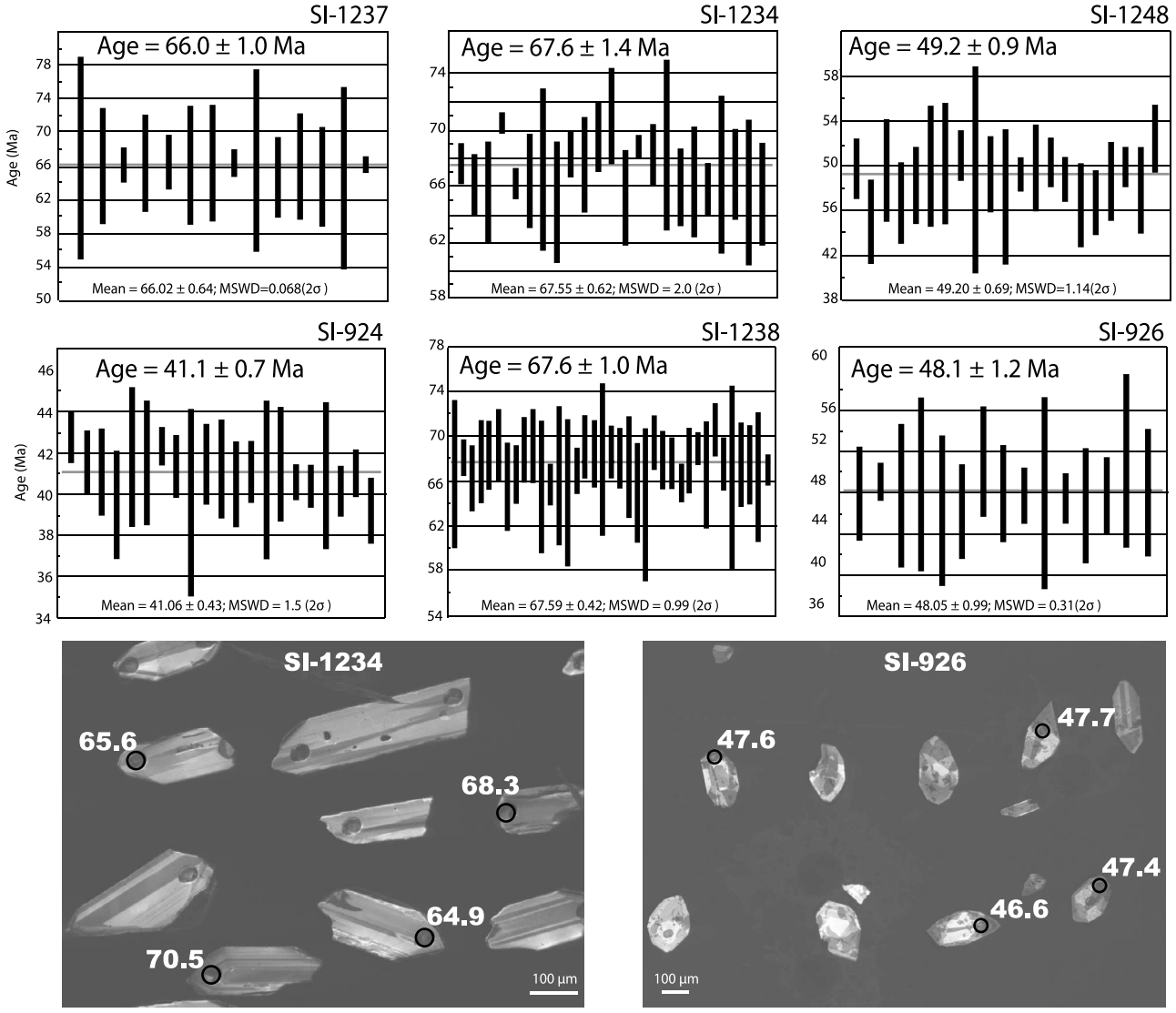

Figure 2. U/Pb ages obtained in six granitoid samples from the Azuero Peninsula and examples of zircons dated below. See Table 1 for sample coordinates and Table 2 for analytical data.

therein], those in the San Blas Range have received comparatively less attention [*Maury et al.*, 1995; *Wegner et al.*, 2011]. Here we collected 19 samples of igneous rocks in the San Blas Range for chemical analyses (Tables 3a and 3b), that combined with field observations allow characterization of the tectono-magmatic evolution of the arc basement and older arc sequences (also referred to as "volcaniclastic basement" thereafter, Figure 3).

[21] The volcaniclastic basement can be geochemically divided into three groups based on distinct contents of immobile trace elements (Figures 4 and 5a). Group I is composed of basalts with a moderately depleted pattern on a primitive mantle-normalized multielement diagram ((La/Sm)N, i.e., primitive mantle-normalized La/Sm = 0.5 to 0.6), a progressive depletion in the more incompatible elements, a small Nb-Ta positive anomaly, and no Ti and Zr-Hf negative anomalies. Group II is composed of basalts characterized by slightly enriched to depleted patterns on a primitive mantle-normalized multielement diagram ((La/Sm)N = 0.5 to 1.1), with small, variable Nb-Ta and Ti negative anomalies. Distinct depletions in the most incompatible elements and Zr-Hf contents are another characteristic of this group. Group III is composed of basaltic-andesitic lavas and intrusives characterized by slightly depleted to enriched patterns on a primitive mantle-normalized multielement diagram ((La/Sm)N = 0.9 to 2.0), with a strong Nb-Ti negative anomaly, and various Ti and Zr-Hf negative anomalies. No systematic change in trace element contents has been observed between the basalts and andesites.

[22] The stratigraphic distribution of geochemical groups in the studied area can be inferred from field, structural and stratigraphic relationships, integrated with geochemical criteria (Figure 3). Important stratigraphic field constraints are provided by dike samples SI-3801 and SI-3797 of Group III, which clearly crosscut the sequences of Group I close to sample SI-3802, and Group II close to sample SI-3796, respectively (see Table 1 and Figure 3). The spatial distribution of lava flows from each group correlates with the structural arrangement of the basement, with group I occurring within outcrops of the lower volcaniclastic basement

Table 2. U/Pb Geochronological Data

		Isotope Ratios									Apparent Ages (Ma)			
Analysis	U (ppm)	$^{206}Pb/^{204}Pb$	U/Th	$^{206}Pb^*/^{207}Pb^*$	± (%)	$^{207}Pb^*/^{235}U^*$	±	$^{206}Pb^*/^{238}U$	± (%)	Error Corr.	$^{206}Pb^*/^{238}U^*$	± (Ma)	$^{207}Pb^*/^{235}U$	± (Ma)
						SI-924								
1	205	1328	0.7	21.6732	24.1	0.0424	24.1	0.0067	1.5	0.06	42.8	0.6	42.1	10.0
2	173	1191	0.8	21.6070	25.4	0.0412	25.5	0.0065	1.8	0.07	41.5	0.8	41.0	10.2
3	140	1047	1.2	20.7012	25.5	0.0426	25.6	0.0064	2.5	0.10	41.1	1.0	42.4	10.6
4	219	1365	0.7	21.6975	23.4	0.0390	23.6	0.0061	3.3	0.14	39.5	1.3	38.9	9.0
5	67	511	1.9	14.3179	35.1	0.0627	35.3	0.0065	4.0	0.11	41.8	1.7	61.7	21.1
6	286	1865	0.8	19.7058	19.6	0.0452	19.9	0.0065	3.6	0.18	41.5	1.5	44.9	8.8
7	273	1669	0.8	21.2069	16.6	0.0428	16.6	0.0066	1.1	0.07	42.3	0.5	42.6	6.9
8	259	1413	1.2	22.5257	26.3	0.0394	26.3	0.0064	1.8	0.07	41.4	0.7	39.2	10.1
9	137	973	1.4	20.3853	23.5	0.0417	24.2	0.0062	5.7	0.24	39.6	2.3	41.4	9.8
12	435	1813	0.9	20.7260	12.9	0.0429	13.1	0.0065	2.3	0.18	41.4	1.0	42.7	5.5
14	225	1573	1.2	28.2469	53.5	0.0313	53.6	0.0064	2.9	0.05	41.3	1.2	31.3	16.5
16	97	829	1.4	21.8526	78.7	0.0397	78.8	0.0063	2.5	0.03	40.5	1.0	39.6	30.6
18	161	1154	1.0	21.1294	22.5	0.0417	22.5	0.0064	1.8	0.08	41.1	0.7	41.5	9.2
19	130	1173	1.3	25.5825	39.7	0.0341	40.0	0.0063	4.7	0.12	40.7	1.9	34.1	13.4
24	152	1043	1.1	19.0524	39.4	0.0467	39.6	0.0064	3.3	0.08	41.4	1.4	46.3	17.9
27	275	1832	0.8	20.6464	12.8	0.0422	12.9	0.0063	1.1	0.08	40.6	0.4	41.9	5.3
29	186	1243	0.9	20.6984	20.6	0.0419	20.6	0.0063	1.3	0.06	40.4	0.5	41.6	8.4
31	123	1125	1.2	25.6602	52.1	0.0320	52.1	0.0059	2.9	0.06	38.2	1.1	32.0	16.4
34	113	910	1.9	18.2631	126.2	0.0481	126.3	0.0064	4.3	0.03	40.9	1.7	47.7	58.9
36	218	1661	1.4	20.5464	12.2	0.0419	12.3	0.0062	1.5	0.12	40.1	0.6	41.7	5.0
38	396	2113	0.7	20.5595	8.8	0.0428	8.9	0.0064	1.4	0.16	41.0	0.6	42.5	3.7
40	339	1861	0.8	19.2273	13.5	0.0437	13.6	0.0061	2.0	0.14	39.2	0.8	43.5	5.8
						SI-926								
1	59	699	3.1	19.1657	193.6	0.0535	193.7	0.0074	4.8	0.02	47.7	2.3	52.9	100.1
2	202	1957	2.5	23.8303	16.8	0.0441	16.9	0.0076	1.9	0.11	48.9	0.9	43.8	7.3
3	111	1018	3.6	25.6101	103.0	0.0399	103.3	0.0074	7.3	0.07	47.6	3.5	39.7	40.3
5	135	2150	1.4	24.4755	122.4	0.0427	122.7	0.0076	8.6	0.07	48.6	4.2	42.4	51.0
6	102	1706	3.4	15.7246	28.4	0.0630	29.5	0.0072	7.9	0.27	46.2	3.6	62.1	17.8
7	90	1051	1.9	30.2254	81.0	0.0327	81.1	0.0072	5.0	0.06	46.0	2.3	32.7	26.1
8	74	1465	2.9	20.2359	219.7	0.0540	219.8	0.0079	5.3	0.02	50.9	2.7	53.4	114.9
9	63	877	2.1	30.0421	62.5	0.0341	62.6	0.0074	4.8	0.08	47.8	2.3	34.1	21.0
10	63	818	2.4	20.4708	148.9	0.0499	148.9	0.0074	2.8	0.02	47.6	1.3	49.5	72.0
11	73	1610	3.3	18.4741	29.6	0.0556	31.2	0.0075	9.8	0.31	47.9	4.7	55.0	16.7
13	125	1554	2.0	19.5827	42.2	0.0519	42.3	0.0074	2.6	0.06	47.4	1.2	51.4	21.2
14	59	903	1.9	24.6012	105.0	0.0407	105.2	0.0073	6.0	0.06	46.6	2.8	40.5	41.8
15	103	1565	3.5	22.0683	50.9	0.0464	51.0	0.0074	3.8	0.07	47.7	1.8	46.0	23.0
16	48	1210	3.6	31.6657	62.9	0.0346	63.4	0.0079	8.3	0.13	51.0	4.2	34.5	21.5
17	51	699	2.8	21.8597	54.7	0.0430	54.9	0.0068	4.0	0.07	43.8	1.7	42.7	23.0
20	114	1284	1.6	17.8783	23.9	0.0575	24.7	0.0075	6.5	0.26	47.9	3.1	56.8	13.6
						SI-1234								
2	88	2195	1.9	26.8984	86.7	0.0541	86.7	0.0105	1.0	0.01	67.6	0.7	53.5	45.2
3	165	3210	1.5	23.3223	17.1	0.0609	17.2	0.0103	1.6	0.09	66.1	1.1	60.1	10.0
4	134	3015	2.4	23.2980	18.0	0.0605	18.2	0.0102	2.7	0.15	65.6	1.8	59.7	10.6
5	333	7975	1.9	22.7469	10.2	0.0666	10.2	0.0110	0.5	0.05	70.5	0.4	65.5	6.5
6	101	3355	2.2	32.1731	59.1	0.0442	59.1	0.0103	0.8	0.01	66.2	0.5	44.0	25.4
7	71	1790	3.1	30.0108	47.5	0.0476	47.5	0.0104	2.5	0.05	66.4	1.6	47.2	21.9
8	147	3145	1.6	20.0075	14.1	0.0722	14.7	0.0105	4.3	0.29	67.2	2.8	70.8	10.1
9	131	2955	2.6	26.7269	31.5	0.0522	31.7	0.0101	3.3	0.10	64.9	2.1	51.7	16.0
60	353	8040	2.3	22.7520	11.8	0.0645	11.9	0.0106	1.2	0.10	68.3	0.8	63.5	7.3
20	215	4430	1.8	20.1522	11.4	0.0721	11.7	0.0105	2.5	0.21	67.6	1.7	70.7	8.0
21	434	9915	2.0	21.6338	6.1	0.0692	6.3	0.0109	1.8	0.28	69.6	1.2	67.9	4.1
23	108	1900	1.9	18.7616	24.3	0.0814	24.4	0.0111	2.4	0.10	71.0	1.7	79.5	18.7
24	111	2440	4.0	26.0812	29.8	0.0537	30.0	0.0102	2.6	0.09	65.2	1.7	53.2	15.5
27	208	4790	3.1	21.6776	13.4	0.0683	13.4	0.0107	0.6	0.04	68.8	0.4	67.1	8.7
28	186	3785	1.6	22.5833	15.1	0.0650	15.2	0.0106	1.6	0.10	68.3	1.1	63.9	9.4
29	101	1925	2.2	28.6654	58.2	0.0517	58.4	0.0108	4.4	0.07	68.9	3.0	51.2	29.2
31	130	2965	3.5	17.9900	25.0	0.0788	25.1	0.0103	2.1	0.08	66.0	1.4	77.1	18.6
32	275	5515	1.6	21.8041	8.0	0.0654	8.5	0.0103	2.9	0.34	66.3	1.9	64.3	5.3
33	200	4065	2.8	23.0783	22.0	0.0613	22.0	0.0103	1.4	0.06	65.8	0.9	60.4	12.9
34	144	2390	1.4	22.3841	15.2	0.0642	15.8	0.0104	4.2	0.26	66.9	2.8	63.2	9.7
35	97	2115	2.0	19.2223	9.0	0.0748	9.3	0.0104	2.4	0.26	66.9	1.6	73.2	6.6
39	112	2780	5.0	15.8329	28.6	0.0890	28.9	0.0102	3.9	0.14	65.6	2.6	86.6	24.0
40	299	6845	2.1	20.1361	14.9	0.0699	15.1	0.0102	2.8	0.18	65.5	1.8	68.6	10.0

Table 2. (continued)

		Isotope Ratios									Apparent Ages (Ma)			
Analysis	U (ppm)	$^{206}Pb/^{204}Pb$	U/Th	$^{206}Pb^*/^{207}Pb^*$	± (%)	$^{207}Pb^*/^{235}U^*$	±	$^{206}Pb^*/^{238}U$	± (%)	Error Corr.	$^{206}Pb^*/^{238}U^*$	± (Ma)	$^{207}Pb^*/^{235}U$	± (Ma)
						SI-1237								
1	86	1180	2.5	18.1598	174.9	0.0790	175.1	0.0104	9.1	0.05	66.8	6.0	77.2	131.0
2	368	1012	2.9	17.1705	39.7	0.0825	40.0	0.0103	5.2	0.13	65.9	3.4	80.5	31.0
3	516	5132	2.4	21.4865	14.1	0.0662	14.2	0.0103	1.5	0.11	66.1	1.0	65.0	9.0
4	503	1704	1.6	14.2818	53.6	0.0997	53.7	0.0103	4.5	0.08	66.2	2.9	96.5	49.5
5	364	3212	1.5	19.7912	14.0	0.0720	14.2	0.0103	2.5	0.17	66.3	1.6	70.6	9.7
6	178	2448	2.6	21.3483	44.7	0.0665	45.1	0.0103	5.4	0.12	66.1	3.6	65.4	28.5
7	2169	9672	1.0	19.2838	8.6	0.0740	10.0	0.0103	5.2	0.51	66.4	3.4	72.5	7.0
8	416	1448	1.3	17.4653	25.0	0.0816	25.0	0.0103	1.2	0.05	66.3	0.8	79.6	19.2
9	1636	13856	1.0	19.2395	28.0	0.0743	29.2	0.0104	8.2	0.28	66.5	5.4	72.8	20.5
11	524	3600	1.1	18.4574	15.9	0.0752	16.3	0.0101	3.7	0.23	64.6	2.4	73.6	11.6
132	149	2420	2.3	28.9531	76.9	0.0489	77.1	0.0103	4.8	0.06	65.9	3.2	48.5	36.5
14	139	2800	3.2	19.7995	69.4	0.0701	69.6	0.0101	4.6	0.07	64.6	3.0	68.8	46.3
15	54	1104	3.2	33.0269	68.1	0.0419	68.6	0.0100	8.4	0.12	64.4	5.4	41.7	28.0
16	355	2852	1.6	21.5001	11.3	0.0660	11.3	0.0103	0.7	0.06	66.0	0.4	64.9	7.1
						SI-1238								
1	75	1295	3.2	26.4028	86.5	0.0492	86.8	0.0094	8.1	0.09	60.5	4.9	48.8	41.4
2	65	1029	3.5	32.9415	72.6	0.0434	72.8	0.0104	5.0	0.07	66.6	3.3	43.2	30.8
3	155	2024	4.1	24.5880	29.1	0.0595	29.1	0.0106	1.1	0.04	68.0	0.8	58.7	16.6
4	118	1761	2.0	23.2279	25.2	0.0613	25.3	0.0103	2.2	0.09	66.2	1.5	60.4	14.8
5	309	4599	2.3	21.8730	11.1	0.0665	11.4	0.0106	2.7	0.24	67.7	1.8	65.4	7.2
6	123	1968	4.3	22.7468	31.9	0.0646	32.0	0.0107	2.2	0.07	68.3	1.5	63.5	19.7
7	125	2068	2.9	23.9392	26.6	0.0622	26.7	0.0108	2.3	0.08	69.3	1.6	61.3	15.9
8	209	3204	1.7	24.5358	23.8	0.0573	24.0	0.0102	3.0	0.12	65.4	1.9	56.6	13.2
9	161	2601	1.9	30.3669	47.9	0.0471	47.9	0.0104	1.9	0.04	66.5	1.3	46.7	21.9
10	170	2660	2.1	19.7964	16.0	0.0747	16.1	0.0107	2.1	0.13	68.8	1.4	73.1	11.4
11	153	2331	2.1	23.4150	26.2	0.0635	26.3	0.0108	2.3	0.09	69.1	1.6	62.5	15.9
12	207	2923	1.7	24.1036	22.3	0.0584	22.8	0.0102	4.5	0.20	65.4	2.9	57.6	12.8
13	133	1980	3.5	20.8687	13.1	0.0676	13.2	0.0102	1.4	0.10	65.7	0.9	66.5	8.5
14	60	847	4.0	17.1519	140.7	0.0832	140.8	0.0104	4.7	0.03	66.4	3.1	81.2	110.3
17	208	4274	2.2	21.4693	19.6	0.0650	20.2	0.0101	5.0	0.25	64.9	3.3	63.9	12.5
18	160	2738	1.9	23.9431	23.8	0.0600	23.9	0.0104	1.5	0.06	66.9	1.0	59.2	13.7
19	234	3326	1.6	22.4969	15.3	0.0659	15.4	0.0108	2.0	0.13	69.0	1.4	64.8	9.7
20	153	2412	2.1	27.5419	38.5	0.0534	38.6	0.0107	2.2	0.06	68.4	1.5	52.8	19.9
21	84	1158	2.8	23.8447	40.1	0.0612	40.4	0.0106	5.0	0.12	67.9	3.4	60.3	23.7
22	257	4040	2.4	22.1930	16.4	0.0664	16.4	0.0107	1.7	0.10	68.5	1.1	65.3	10.4
23	226	3152	2.9	23.3322	19.7	0.0627	19.7	0.0106	1.9	0.10	68.0	1.3	61.7	11.8
24	59	910	1.6	22.2219	36.8	0.0650	37.0	0.0105	3.3	0.09	67.2	2.2	64.0	22.9
25	283	2794	2.3	15.9242	34.7	0.0876	34.9	0.0101	3.4	0.10	64.9	2.2	85.3	28.5
26	111	1769	2.2	21.4779	28.8	0.0639	29.3	0.0099	5.3	0.18	63.8	3.4	62.9	17.8
27	193	3530	3.3	24.3239	33.1	0.0613	33.2	0.0108	1.7	0.05	69.4	1.2	60.5	19.5
28	101	1236	2.4	24.7495	39.8	0.0589	39.8	0.0106	1.9	0.05	67.8	1.3	58.1	22.5
29	128	1809	4.5	26.6023	38.0	0.0546	38.1	0.0105	1.7	0.04	67.6	1.1	54.0	20.0
30	258	4355	2.4	21.5760	9.7	0.0656	9.8	0.0103	1.3	0.13	65.8	0.8	64.5	6.1
31	395	5976	2.5	19.5214	9.1	0.0747	9.3	0.0106	2.1	0.23	67.8	1.4	73.2	6.6
32	254	3948	3.6	21.7882	12.9	0.0679	12.9	0.0107	1.0	0.08	68.8	0.7	66.7	8.3
33	66	1166	2.8	23.7892	41.5	0.0601	41.6	0.0104	3.6	0.09	66.5	2.4	59.2	24.0
34	189	2930	4.2	22.8712	18.2	0.0663	18.3	0.0110	1.7	0.09	70.5	1.2	65.2	11.6
35	704	8584	1.8	20.8440	4.1	0.0696	4.5	0.0105	1.7	0.39	67.5	1.2	68.4	2.9
36	51	803	2.4	21.1927	32.1	0.0667	32.8	0.0103	6.6	0.20	65.8	4.3	65.6	20.8
37	179	2786	3.4	20.2913	13.9	0.0714	14.2	0.0105	2.7	0.19	67.4	1.8	70.0	9.6
38	381	5927	1.8	21.5680	6.8	0.0672	7.2	0.0105	2.6	0.36	67.4	1.7	66.1	4.6
39	107	1769	4.1	18.7762	31.2	0.0759	31.5	0.0103	4.4	0.14	66.3	2.9	74.3	22.6
40	187	3175	3.8	20.7391	6.4	0.0694	6.5	0.0104	1.0	0.15	66.9	0.7	68.1	4.3
						SI-1248								
1	111	1018	2.1	21.1727	32.1	0.0504	32.2	0.0077	2.7	0.08	49.7	1.3	49.9	15.7
3	111	962	1.8	23.2129	51.0	0.0417	51.2	0.0070	4.2	0.08	45.1	1.9	41.4	20.8
4	71	936	2.5	22.0054	64.8	0.0437	65.0	0.0070	5.1	0.08	44.8	2.3	43.4	27.6
5	94	944	1.7	16.6005	327.3	0.0642	327.3	0.0077	4.6	0.01	49.6	2.3	63.1	203.0
6	134	1380	2.1	17.7919	20.7	0.0563	21.0	0.0073	3.9	0.18	46.7	1.8	55.6	11.4
8	128	1029	1.5	20.6283	25.8	0.0503	26.1	0.0075	3.5	0.14	48.3	1.7	49.8	12.7
9	114	1254	2.3	21.7975	31.9	0.0492	32.4	0.0078	5.4	0.17	49.9	2.7	48.8	15.4
10	106	1254	2.3	21.3570	23.2	0.0506	23.8	0.0078	5.3	0.22	50.3	2.6	50.1	11.6
11	109	1236	2.7	18.5731	40.7	0.0589	40.8	0.0079	2.2	0.05	51.0	1.1	58.1	23.1
12	97	1077	2.1	30.5127	39.7	0.0349	40.8	0.0077	9.3	0.23	49.6	4.6	34.9	14.0
13	118	958	2.4	25.5541	119.1	0.0414	119.2	0.0077	3.5	0.03	49.2	1.7	41.1	48.1
14	138	1310	1.9	31.1627	41.0	0.0325	41.5	0.0073	6.4	0.15	47.2	3.0	32.5	13.3

Table 2. (continued)

		Isotope Ratios									Apparent Ages (Ma)			
Analysis	U (ppm)	$^{206}Pb/^{204}Pb$	U/Th	$^{206}Pb^*/^{207}Pb^*$	± (%)	$^{207}Pb^*/^{235}U^*$	±	$^{206}Pb^*/^{238}U$	± (%)	Error Corr.	$^{206}Pb^*/^{238}U^*$	± (Ma)	$^{207}Pb^*/^{235}U$	± (Ma)
15	137	892	1.9	17.7229	34.6	0.0597	34.7	0.0077	1.5	0.04	49.3	0.7	58.9	19.8
17	133	1702	1.5	20.6019	41.8	0.0466	42.5	0.0070	7.4	0.18	44.8	3.3	46.3	19.2
18	165	1613	1.5	16.6796	19.9	0.0641	20.3	0.0078	3.8	0.19	49.8	1.9	63.1	12.4
20	114	1162	2.1	20.9081	40.6	0.0516	40.7	0.0078	2.2	0.05	50.3	1.1	51.1	20.3
21	230	1832	1.2	19.6977	15.8	0.0532	15.9	0.0076	2.0	0.12	48.8	1.0	52.6	8.1
22	96	1018	2.2	24.9204	50.3	0.0400	50.5	0.0072	4.0	0.08	46.5	1.8	39.9	19.7
25	87	1003	2.3	36.9179	89.1	0.0272	89.2	0.0073	3.0	0.03	46.7	1.4	27.2	23.9
27	127	1095	1.7	34.8858	92.8	0.0299	92.9	0.0076	3.6	0.04	48.6	1.7	29.9	27.4
28	150	1772	1.6	26.9160	68.5	0.0398	68.6	0.0078	1.8	0.03	49.9	0.9	39.7	26.7
29	78	851	2.5	16.8300	150.2	0.0610	150.3	0.0074	4.0	0.03	47.8	1.9	60.1	88.0
30	84	803	2.5	18.0020	120.3	0.0625	120.3	0.0082	2.9	0.02	52.4	1.5	61.6	72.0

characterized above; groups II and III sequentially in the core and in the limbs of the asymmetric anticline defined above and corresponding to the middle part of the volcaniclastic basement (Figure 3). These observations indicate a consistent stratigraphic arrangement of the groups in the volcaniclastic basement complex with, from bottom to top, groups I, II and III. An existing geochemical data set obtained from igneous rocks in the nearby Chagres Basin [*Wegner et al.*, 2011] can be also subdivided into Groups I, II and III using same criteria as above (Figure 5a).

[23] In summary, three distinctive geochemical groups, from oceanic plateau to supra-subduction arc, can be discriminated using enrichment/depletion patterns on multielement diagrams, and Nb-Ti anomalies. The high compositional similarity between our geochemical samples and those of *Wegner et al.* [2011] in the Chagres Basin, and *Buchs et al.* [2010] in the Azuero Peninsula, along with the geochronological data on intermediate plutons described in a previous section, support the inference that the San Blas Range and the Azuero Peninsula are part of the same belt in central Panama, albeit exposing different crustal levels. Oceanic plateau sequences occur regionally at the base of this belt, but so far have only been recognized in a few outcrops in eastern Panama possibly due to significant burial under younger arc deposits.

5.3. Paleomagnetism

[24] Paleomagnetic sampling in central Panama targeted basaltic and sedimentary sequences of the volcaniclastic basement above described (Figure 3). Sampling was performed along an approximately 100 km-long, east-west transect, in three main areas with exposures of ocean-floor sequences (Figure 3): 1) riverbed outcrops along the Mamoni-Terable rivers; 2) freshly cut outcrops along the Panama-Colon old highway, both north and south of the Rio Gatun Fault; and 3) additional sites in nearby areas to assess Oligocene (Quebrancha Syncline, Panama-Colon old highway), middle Miocene (Canal area) and uppermost Miocene to recent magnetization directions (El Valle Volcano, Figure 1).

[25] Outcrops in the Mamoni-Terable riverbeds and along the Panama-Colon old highway contain reliable pelagic sedimentation bedding data and mafic volcanic rocks within folded structures. We sampled in lithologically similar basaltic sequences, thought to represent coeval deposits (Figure 3). Field sites were chosen on the basis of reliability

Table 3a. XRF Analyses

		Major Elements (wt%)												
Sample	Group	SiO_2	TiO_2	Al_2O_3	Fe_2O_3	MnO	MgO	CaO	Na_2O	K_2O	P_2O_5	SO_3	LOI	SUM
SI-3802	I	47.13	1.31	13.59	12.98	0.18	7.86	10.46	2.67	0.08	0.13	0.03	3.92	100.33
SI-9173	I	43.95	1.02	12.18	12.68	0.15	5.31	9.64	3.93	0.04	0.08	0.18	10.95	100.10
SI-2685	IIa	50.40	0.98	14.67	9.60	0.17	8.86	10.74	2.61	0.30	0.08	bdl	1.76	100.16
SI-3793	IIa	49.25	1.08	15.83	8.77	0.26	9.82	10.64	2.19	0.15	0.08	0.14	2.18	100.38
SI-3796	IIb	41.83	0.75	13.06	10.11	0.20	9.77	9.63	2.82	0.05	0.12	bdl	11.75	100.08
SI-2688	IIIa	60.88	1.54	14.83	6.77	0.08	2.57	5.85	5.32	0.17	0.29	bdl	1.79	100.07
SI-2690	IIIa	47.55	0.89	16.54	11.69	0.16	8.11	11.13	2.07	0.13	0.05	bdl	1.55	99.88
SI-2693	IIIa	45.92	1.18	17.16	11.09	0.11	9.21	8.93	2.55	0.25	0.14	bdl	3.53	100.06
SI-3754	IIIa	59.11	1.31	12.77	12.29	0.13	4.46	3.30	4.34	0.11	0.15	bdl	2.19	100.14
SI-3756	IIIa	51.55	0.99	17.59	11.20	0.18	4.96	10.02	2.77	0.48	0.14	0.11	0.71	100.68
SI-3758	IIIa	46.39	1.34	17.84	17.33	0.15	3.03	8.75	0.73	2.29	0.15	1.88	2.04	101.91
SI-3797	IIIa	47.82	1.03	13.76	8.43	0.14	4.97	9.79	4.35	0.10	0.11	1.11	8.06	99.65
SI-3764	IIIa	50.14	0.32	15.49	7.08	0.13	7.11	8.73	2.00	0.25	0.05	bdl	6.83	98.14
SI-2655	IIIa	58.24	0.53	18.02	8.14	0.19	3.06	7.17	3.19	0.64	0.12	bdl	1.11	100.41
SI-2664	IIIa	50.67	0.86	16.63	10.70	0.19	6.51	8.87	2.34	2.08	0.08	bdl	1.48	100.40
SI-3801	IIIb	50.58	0.90	14.40	11.85	0.20	6.52	6.89	5.21	0.12	0.18	bdl	3.22	100.05
SI-3805	IIIb	49.28	0.82	16.74	11.00	0.14	4.92	4.89	5.93	0.19	0.19	0.02	5.99	100.10
SI-2658	IIIb	56.73	0.38	17.16	8.09	0.12	5.12	8.21	2.35	0.17	0.10	bdl	1.32	99.74
SI-3886	IIIb	50.45	1.28	17.41	9.36	0.21	3.30	8.16	2.71	1.60	0.25	bdl	4.97	99.71

Table 3b. LA-ICP-MS Analyses

	Trace Elements (ppm)																														
Sample	Sc	Ti	V	Cr	Mn	Ni	Cu	Zn	Ga	Rb	Sr	Y	Zr	Nb	Ba	La	Ce	Pr	Nd	Sm	Eu	Gd	Tb	Dy	Ho	Er	Tm	Yb	Lu	Hf	Ta	Pb	Th	U
SI-3802	57.42	9117.44	434.88	113.51	1341.50	50.78	146.74	74.44	16.21	0.88	147.72	34.95	78.25	2.76	32.74	2.65	7.55	1.31	7.88	3.12	1.14	4.46	0.82	6.15	1.34	4.00	0.60	4.01	0.62	2.19	0.18	0.30	0.25	0.09
SI-9173	60.92	7746.84	401.83	150.58	1205.12	79.11	145.44	82.98	14.78	1.15	114.72	28.68	59.23	2.64	90.63	2.51	6.77	1.14	6.52	2.53	0.97	3.68	0.70	5.22	1.11	3.43	0.50	3.39	0.51	1.69	0.17	0.36	0.19	0.06
SI-2685	47.84	6411.82	256.37	714.14	1275.12	322.99	91.70	41.24	11.19	2.94	197.02	20.86	66.61	0.73	67.46	2.18	6.75	1.20	7.03	2.54	0.90	3.10	0.53	3.73	0.80	2.32	0.35	2.33	0.33	1.62	0.05	0.93	0.07	0.05
SI-3793	52.53	7037.13	269.76	395.30	1861.18	110.78	80.15	42.89	12.49	1.77	178.09	24.17	75.23	0.83	43.20	2.35	7.27	1.33	7.92	2.91	1.10	3.54	0.61	4.33	0.91	2.72	0.39	2.61	0.39	1.82	0.06	0.58	0.08	0.03
SI-3796	52.36	5618.95	329.54	644.91	1606.35	168.04	64.75	83.38	13.68	0.81	64.92	15.37	51.55	2.95	29.28	4.67	10.92	1.75	9.07	2.64	0.85	2.78	0.44	2.94	0.60	1.76	0.26	1.73	0.26	1.44	0.18	1.82	0.39	0.13
SI-2688	33.69	10353.12	338.05	16.79	604.65	15.30	23.25	30.00	11.71	1.96	362.21	35.63	162.34	2.58	142.30	11.19	25.83	4.02	20.95	5.88	1.71	6.13	0.96	6.51	1.33	3.92	0.57	3.73	0.55	4.16	0.16	1.26	1.31	0.70
SI-2690	56.55	5880.12	381.63	244.51	1186.40	81.68	133.53	62.07	14.10	1.23	245.76	12.61	56.20	0.67	71.91	2.98	6.31	0.97	5.17	1.64	0.67	2.00	0.32	2.33	0.49	1.41	0.22	1.42	0.21	1.42	0.04	0.80	0.33	0.09
SI-2693	43.98	7815.74	320.04	102.54	769.64	54.55	121.87	61.01	16.01	2.98	326.53	30.28	97.94	1.60	123.85	7.24	16.21	2.61	14.01	4.30	1.51	4.89	0.78	5.39	1.10	3.25	0.49	3.44	0.55	2.63	0.10	1.40	0.58	0.22
SI-3754	44.49	8530.60	466.10	10.33	901.79	12.55	254.33	68.26	10.67	1.39	172.57	28.28	62.75	0.85	37.95	5.04	11.74	1.96	10.91	3.52	1.25	4.28	0.71	5.14	1.08	3.14	0.48	3.03	0.45	1.87	0.05	0.74	0.62	0.16
SI-3756	44.64	6656.05	350.35	27.37	1291.33	26.30	123.82	57.80	15.74	5.99	327.68	25.93	85.21	1.37	300.25	7.41	16.02	2.55	13.14	3.79	1.19	4.15	0.67	4.70	1.00	2.93	0.43	2.94	0.43	2.25	0.08	1.18	1.08	0.26
SI-3758	49.66	9042.96	521.14	7.47	1091.93	32.38	45.12	104.11	20.04	32.27	157.37	31.63	76.40	0.83	1408.36	6.06	13.23	2.27	12.16	3.84	0.87	4.49	0.77	5.60	1.21	3.77	0.55	3.75	0.57	2.28	0.05	2.20	0.72	0.22
SI-3797	43.74	7511.61	363.28	96.27	1084.32	46.61	124.15	97.26	15.14	1.29	246.15	24.15	64.84	1.17	70.27	4.38	10.06	1.67	9.41	3.02	1.21	3.72	0.64	4.43	0.92	2.75	0.41	2.66	0.38	1.85	0.08	3.10	0.33	0.10
SI-3764	42.29	2272.82	227.65	419.20	1047.54	108.91	80.09	48.49	12.66	3.63	229.40	12.98	26.77	0.63	196.78	2.90	6.01	0.86	4.25	1.28	0.45	1.63	0.29	2.12	0.46	1.42	0.22	1.53	0.24	0.75	0.04	1.46	0.35	0.12
SI-2655	57.49	10527.28	599.73	8.22	1261.76	37.92	57.28	118.54	22.94	35.37	176.26	35.20	86.06	0.94	1520.26	6.58	14.37	2.45	13.11	4.22	0.95	4.95	0.85	6.16	1.33	4.15	0.60	4.12	0.64	2.52	0.06	2.31	0.80	0.25
SI-2664	47.41	5817.49	311.72	119.52	1370.44	58.98	110.03	55.37	14.11	31.76	281.43	21.57	71.76	1.04	354.55	4.24	9.94	1.54	8.04	2.54	0.81	3.13	0.54	3.90	0.83	2.45	0.37	2.56	0.39	1.86	0.06	1.25	0.80	0.23
SI-3801	54.45	6064.18	394.05	85.63	1416.36	25.30	153.93	68.39	14.22	2.16	175.81	16.62	43.28	1.74	40.12	7.55	16.93	2.52	12.46	3.16	0.95	3.07	0.48	3.18	0.65	1.85	0.27	1.80	0.26	1.30	0.10	0.53	0.76	0.26
SI-3805	41.33	6110.70	439.80	17.56	1073.91	27.56	156.91	74.20	16.40	2.72	248.49	18.33	66.75	1.61	55.11	11.02	23.79	3.65	18.28	4.66	1.40	4.22	0.59	3.59	0.71	2.00	0.29	1.91	0.28	1.78	0.09	0.81	1.21	0.35
SI-2658	41.99	2616.97	290.65	60.01	855.72	16.08	43.17	57.03	13.84	1.94	476.55	13.01	55.68	1.63	378.79	7.35	14.20	2.09	9.80	2.37	0.68	2.32	0.34	2.29	0.48	1.48	0.22	1.62	0.26	1.57	0.10	3.04	1.24	0.39
SI-3886	32.21	9183.31	308.27	16.51	1634.43	12.68	167.67	74.01	18.30	29.42	479.67	39.20	176.83	9.81	801.21	18.79	36.07	5.03	23.35	6.03	1.65	6.15	1.01	7.00	1.45	4.25	0.63	4.09	0.61	4.53	0.61	4.06	3.03	0.94
Standard (BCR-2)	36.76	14652.61	405.10	14.62	1486.89	11.97	17.85	154.90	22.20	47.50	351.98	34.30	187.53	13.39	720.97	26.15	53.20	6.76	29.94	6.98	2.03	6.64	1.01	6.61	1.32	3.73	0.54	3.58	0.51	4.76	0.85	11.40	6.29	1.61

of structural control, lithology and availability of fresh rock exposures along rivers and new highway cuts. Fault zones and secondary veins were avoided as much as possible.

[26] A total of 24 sites were studied, for a total of 192 samples running through demagnetization processes (Table 4). Univectorial and mutivectorial paths of demagnetization were commonly observed. Low-temperature (<300°C) or coercivity (<20 mT) components were uncovered in seven sites (e.g., Figures 6d and 6f), but directions of those low-temperature components are scattered (Table 4). In the next paragraphs we describe paleomagnetic components isolated in middle to high temperature or coercivities (Table 4) for each geographic area.

5.3.1. Mamoni-Terable Rivers

[27] Ten paleomagnetic sites with 65 oriented cores are distributed in outcrops of the ocean-floor sequence in the Mamoni and Terable area (Figure 3). Seven sites were collected in diabase, basalt flows, pillow basalts and tuffaceous volcaniclastic beds interbedded with siliceous mudstone, micrite and calcareous sandstones in the Mamoni-Terable rivers. The other three sites were sampled in andesitic to basaltic dikes (one site) cutting the volcaniclastic basement (two sites). Two components were uncovered in this area. The first component, isolated in two sites at unblocking temperatures <400°C, records northern declinations and moderate positive inclinations that increase after tilt correction (Figure 6g and Table 4). The second, or the characteristic component (C2 in Table 4), was isolated in eight sites at unblocking temperatures lower than 600°C or 100 mT. The characteristic component has northeastern declinations (between 72.1° ± 10.6° and 31.3° ± 1.9°) that record large to moderate clockwise vertical-axis rotations, and positive and negative inclinations all of which become negative after tilt correction (Figures 6c and 6i and Table 4). These results admit two interpretations due to the near equatorial position: a moderate clockwise vertical-axis rotation, or a very large anti-clockwise rotation. We favor the first option (moderate clockwise) because the overall trend of the Campanian to Eocene magmatic axis bends from nearly east-west to northwest-trending (i.e., the alignment of similar plutonic bodies in segment 2 of the Isthmus, Figure 1).

5.3.2. North of Rio Gatun Fault

[28] Four paleomagnetic sites fall north of the Rio Gatun Fault (Figure 3) for a total of 42 oriented cores. Three sites were collected in stratified and lapilli tuff, basaltic lavas, and pelagic siliceous mudstone beds. The remaining site, not considered for statistical analysis, was collected in a massive basalt flow where bedding was poorly defined by red euhedral crystals and amygdules. Paleomagnetic components with westerly declinations were isolated at unblocking temperatures lower than 620°C or 100 mT in 2 sites (275° ± 3.5 and 302° ± 3.1, Figure 6a and Table 4). Declinations of site LI-020089 showed all the samples with easterly declination (113° ± 7.9) and shallow positive inclination, as well as some samples in site LI-020048. Those easterly declinations were considered to indicate reversed polarity with westerly declinations, and for tilt-correction analysis they were converted to westerly directions. These declinations indicate large counterclockwise vertical-axis rotations. Inclinations become negative after tilt correction for the three sites with reliable bedding control (Figure 6i and Table 4).

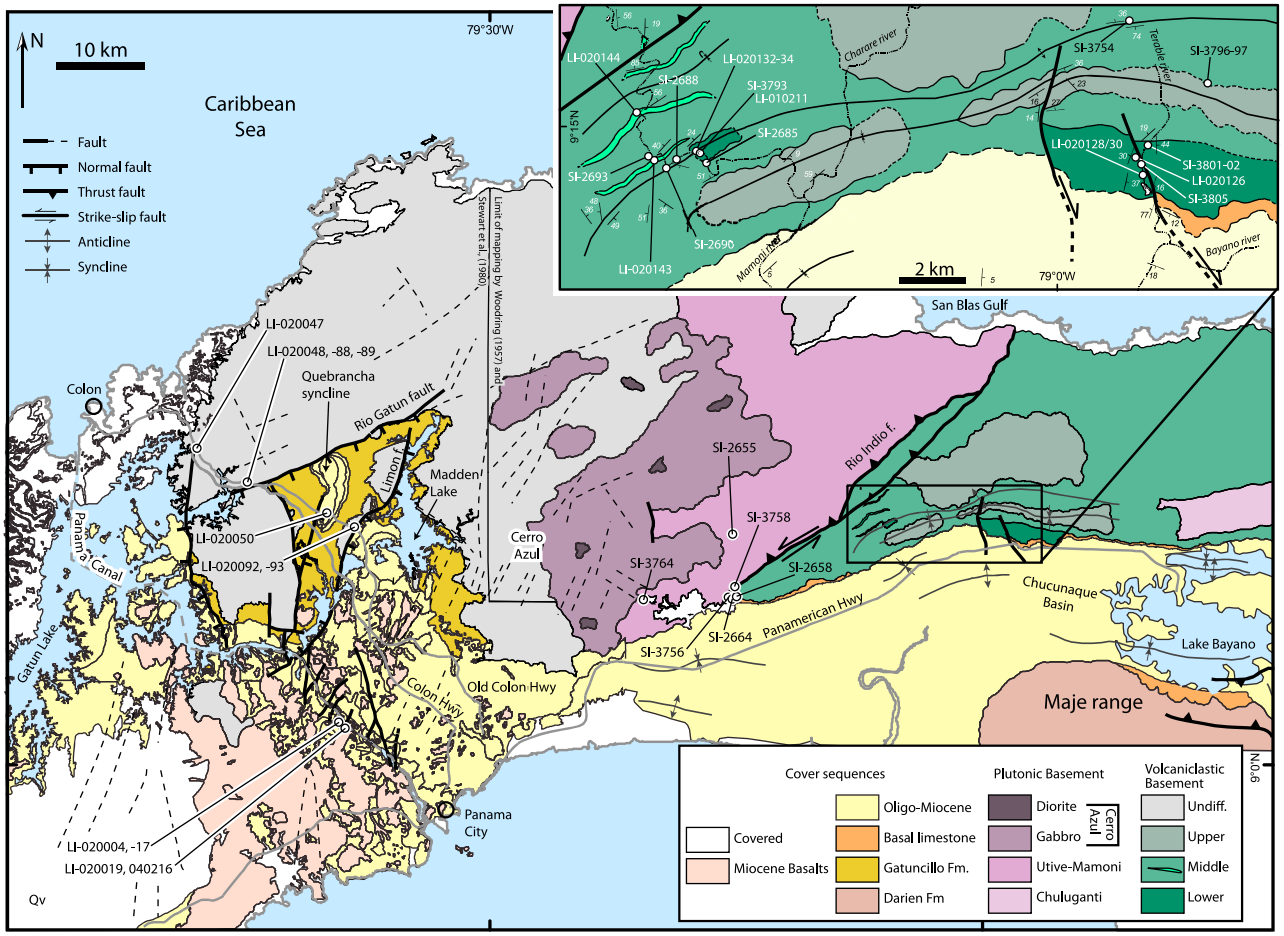

Figure 3. Geologic map of east Panama (modified from *Montes et al.* [2012]) with geochemical sample locations (SI-) and paleomagnetic (LI-) sampling sites. See Table 1 for coordinates.

5.3.3. South of Rio Gatun Fault

[29] A total of three sites and 29 cores were analyzed south of Rio Gatun Fault. Two sites were collected in tuff to lapilli volcaniclastic beds interbedded with andesitic to basaltic lavas of the volcaniclastic basement (Figure 3). The other site was sampled on Oligocene tuffaceous calcareous fossiliferous fine-grained sandstone beds of the cover sequences. Components isolated in the volcaniclastic basement record northeasterly declinations with positive inclinations before tilt correction, but become negative after tilt correction. Declinations in these sites record moderate clockwise vertical-axis rotations (38.6° ± 5.4 and 41.8° ± 1.8, Figures 6b and 6i and Table 4). In Oligocene tuffaceous strata, the characteristic component was isolated at 560°C or 80 mT with a northerly declination and positive moderate inclination before tilt correction, becoming shallower and positive after tilt correction. Declination in this sample indicates little to no vertical-axis rotation (346.7° ± 12.5, Figures 6d and 6h and Table 4).

5.3.4. Canal Basin

[30] Two sites were sampled in the Canal Basin (Figure 3), in lithic to vitric tuffaceous beds interbedded with massive mudstone and sandstone of the Cucaracha Formation, and two sites in layered basalts at the base of the Pedro Miguel Formation (both middle Miocene [*Woodring*, 1957]). Characteristic components uncovered at 660°C or 100 mT show southerly declinations (between 186.3° ± 10.3 and 142.7° ± 10.6) with shallow negative inclinations for the Cucaracha Formation, and positive inclinations for the Pedro Miguel Formation (Figure 6e). After tilt correction, inclinations become moderately negative to very shallow and positive (Figure 6h and Table 4). Declinations in middle Miocene strata of the Canal Bains suggest little to no vertical-axis rotations.

5.3.5. El Valle Volcano

[31] El Valle Volcano is the easternmost active volcano of the Central America volcanic arc with Quaternary activity. Two pulses of volcanic activity have been documented [*de Boer et al.*, 1991; *Defant et al.*, 1991a]: the first is from 10 to 5 Ma, consisting of andesitic to dacitic lava flows, while the younger is related to the emplacement of a dacitic dome and deposition of dacitic pyroclastic flows at 0.9–0.2 Ma. Three sites were located in an andesitic lava flow (Piedra, 6.92 Ma), a proximal extra-caldera volcanic breccia (El Hato, 0.9–0.2 Ma), and in a distal extra-caldera volcaniclastic mudstone beds (ca 0.2 Ma) of the El Valle Volcano (Figure 1). These sites document latest Miocene to recent magnetization directions in Central Panama. Characteristic components uncovered had unblocking temperatures lower than 640°C or 100 mT. The distal extra-caldera site has

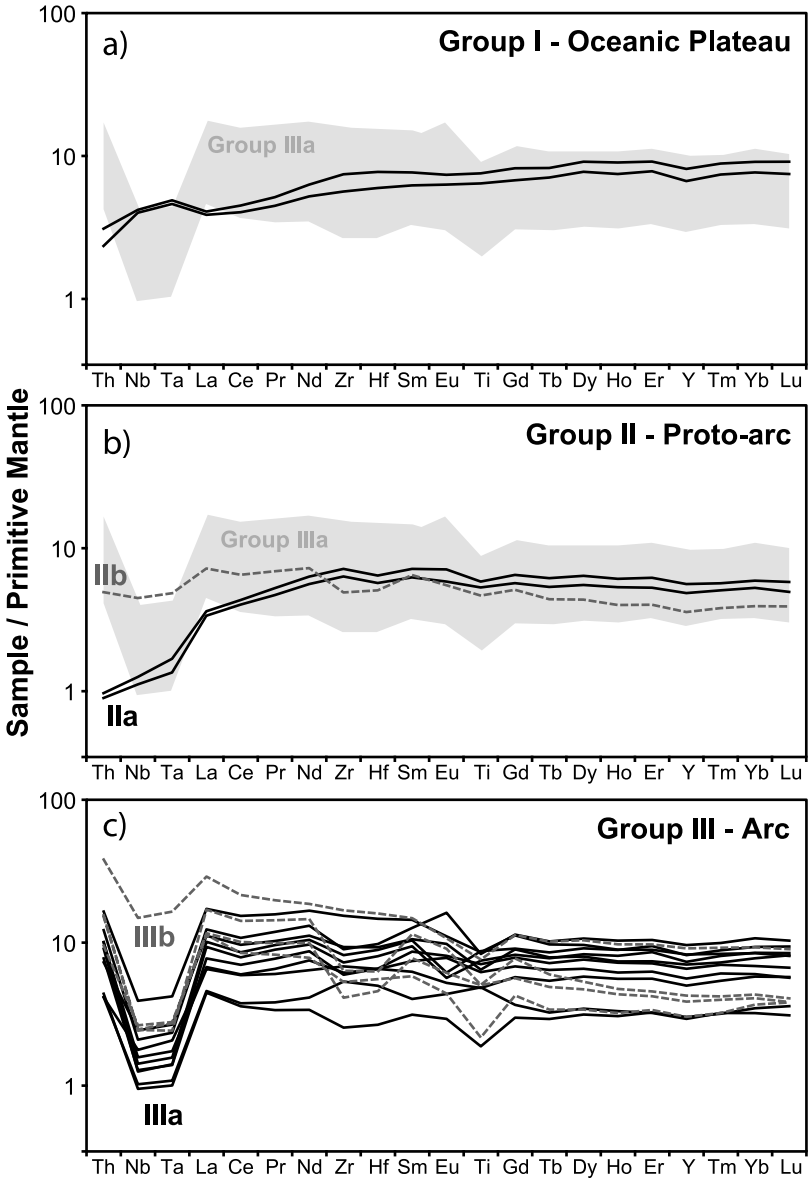

Figure 4. Primitive mantle-normalized multielement diagrams displaying geochemical groups defined in the igneous basement of central Panama (San Blas Range).

north-northwestern declination and shallow positive inclination before and after tilt correction. Proximal extra-caldera and andesitic lava flow sites have southerly declinations with negative inclinations after tilt correction (Figures 6f and 6g and Table 4). Together, these sites document no vertical-axis rotations (178.9° ± 6.9, 169.3° ± 7.6, and 350.1° ± 6.3).

5.3.6. Paleomagnetic Components

[32] Characteristic paleomagnetic directions described above can be grouped into three main components: Late, Middle and Early components. A Late component (A or Ar for reversal in Tables 4 and 5) is defined by a northward and shallow positive (and its reversed) inclination direction

Figure 5. Selected geochemical diagrams showing compositional analogy of the igneous basement of the Central American Arc between south Costa Rica and east Panama, with the occurrence of oceanic plateau, proto-arc and arc-related igneous rocks. (a) La/SmN vs Nb/LaN diagram (N = primitive mantle-normalized). (b) MgO vs TiO2 diagram. (c) TiO2 vs FeO*/MgO diagram (low-, medium-, and high-Fe subdivisions after *Arculus* [2003]; FeO* = total iron oxides expressed as FeO). Chemical groups of central Panama are defined here based on new personal data (larger symbols, see also Figure 4) and data by *Wegner et al.* [2011] from the Chagres Basin. Other data includes: arc sequences from the Rio Morti (east Panama) [*Maury et al.*, 1995]; oceanic plateau, proto-arc and arc sequences from the Azuero area (west Panama) [*Buchs et al.*, 2010]; proto-arc sequences from the Golfito area (south Costa Rica) [*Buchs et al.*, 2010]; MORB (Mid-Ocean Ridge Basalt) data from the East Pacific Rise (EPR) (GEOROC, online chemical database, http://georoc.mpch-mainz.gwdg.de/georoc/, 2010); OIB (Ocean Island Basalt) data from the Quepos accreted island in Costa Rica [*Hauff et al.*, 2000].

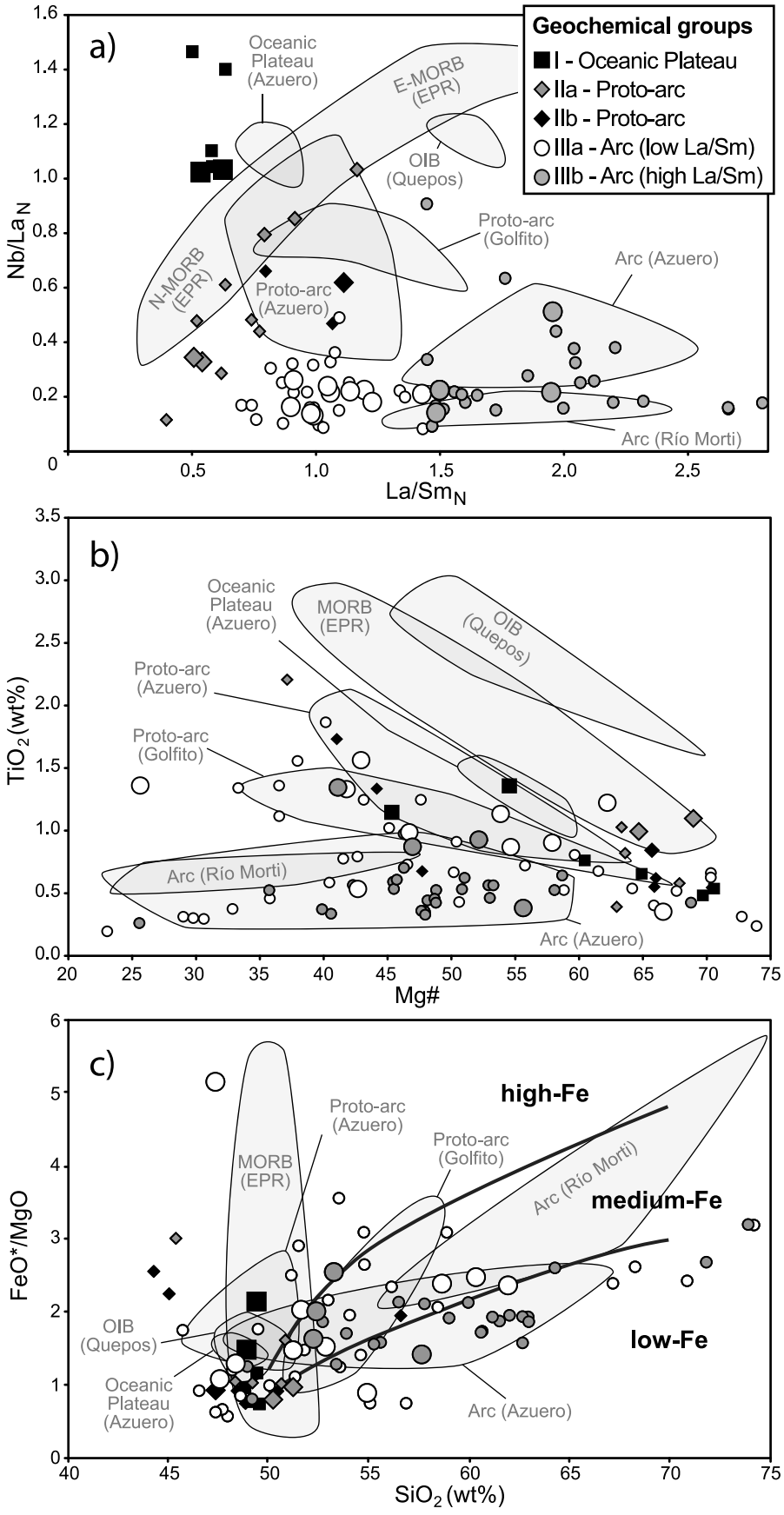
a)
Geochemical groups
I - Oceanic Plateau
IIa - Proto-arc
IIb - Proto-arc
IIIa - Arc (low La/Sm)
IIIb - Arc (high La/Sm)
Oceanic Plateau (Azuero)
E-MORB (EPR)
OIB (Quepos)
Proto-arc (Golfito)
Arc (Azuero)
N-MORB (EPR)
Proto-arc (Azuero)
Arc (Río Morti)
Nb/La_N
La/Sm_N
b)
Oceanic Plateau (Azuero)
MORB (EPR)
OIB (Quepos)
Proto-arc (Azuero)
Proto-arc (Golfito)
Arc (Río Morti)
Arc (Azuero)
TiO2 (wt%)
Mg#
c)
high-Fe
medium-Fe
low-Fe
Proto-arc (Azuero)
Proto-arc (Golfito)
MORB (EPR)
Arc (Río Morti)
OIB (Quepos)
Oceanic Plateau (Azuero)
Arc (Azuero)
FeO*/MgO
SiO2 (wt%)

Figure 5

Table 4. Mean-Site Directions of Characteristic Components

Sample	Unit	Age	Bedding, Dip Azimuth/Dip	Component	N/n	Demag. Range AF (mT)	Demag. Range Thermal (°C)	Before Tilt Correction Dec	Before Tilt Correction Inc	After Tilt Correction Dec	After Tilt Correction Inc	a95	k
				North of Rio Gatun Fault									
LI-020047[a]	Volcaniclastic basement	Late Cretaceous	278/22[b]	C1[b]	7/7	20–100	400–620	263.1	26.6	264.6	5.3	3.5	292.35
LI-020048	Volcaniclastic basement	Paleogene	288/56	C1	16/10	10–100	250–620	273.7	33.9	275.4	−20.8	10.9	20.46
LI-020088	Volcaniclastic basement	Paleogene	282/53	C1	7/7	5–100	450–600	305.8	35.1	302	−14.6	3.1	371.33
LI-020089[a]	Volcaniclastic basement	Paleogene	145/16	C1r	12/9	20–80	350–580	111.2	18.3	113	4.8	7.9	43.74
				South of Rio Gatun Fault									
LI-020050[a]	Oligo - Miocene	Oligocene	320/25	B	8/8	10–80	200–560	352.3	35	346.7	13.1	12.5	20.73
LI-020092	Volcaniclastic basement	Late Cretaceous	330/26	C2	13/10	10–70	300–600	39.1	5.8	38.6	−3.7	5.4	79.8
LI-020093	Volcaniclastic basement	Late Cretaceous	111/52	C2	8/8	10–70	400–600	46.3	5.8	41.8	−15.8	1.8	952.72
				Canal									
LI-020004[a]	Cucaracha Fm.	Middle Miocene (14–17 Ma)	170/31	Br	7/7	15–100	250–560	183.4	−4.5	186.3	−34.5	10.3	35.02
LI-020017	Pedro Miguel Fm.	Middle Miocene	176/29	Br	6/6	30–100	300–540	151.1	9.5	150.3	−16.9	8.5	62.88
LI-040216	Cucaracha Fm.	Middle Miocene (14–17 Ma)	138/30	Br	7/5	15–100	200–590	147	−10.8	149.6	−40.3	4.4	298.56
LI-020019	Pedro Miguel Fm.	Middle Miocene	161/52	Br	6/6	15–100	300–660	129.6	53.1	142.7	5.1	10.6	41.06
				El Valle									
LI-020051[a]	Piedra	Upper Miocene	164/36	Ar	12/7	≤70	300–640	174.2	−12.6	178.9	−47.8	6.9	78.54
LI-020052[a]	Proximal, extra-caldera	Pleistocene	194/18[c]	Ar	8/8	10–100	300–640	170.3	0.2	169.3	−16.2	7.6	54.57
LI-020053[a]	Distal, extra-caldera	Pleistocene	340/07[c]	A	10/9	≤70	≤620	350.4	13.5	350.1	6.6	6.3	67.09
				Mamoní									
LI-010211	Volcaniclastic basement	42–66 Ma	151/25	C2	8/6	5–100	400–580	73.1	−5.1	69.8	−9.8	7.3	84.2
LI-020132	Volcaniclastic basement	42–66 Ma	161/27	C2	7/7	10–100	200–560	62.4	−11.7	58	−6.5	5.5	120.7
LI-020133	Volcaniclastic basement	42–66 Ma	161/27 (bed) 109/67 (dyke)	A	6/4	—	0–400	5.6	24.3	15.5	48	4.4	427.9
LI-020134	Volcaniclastic basement	42–66 Ma	145/35	C2	8/8	5–90	300–600	66.7	−11.6	57.8	−16.2	8	48.76
LI-020143	Volcaniclastic basement	42–66 Ma	58/17	A	8/8	≤35	0–400	5.6	15.6	8	4.9	8.2	46.3
LI-020143			58/17	C2[d]	8/4	—	400–560	60.9	−17.7	61.4	−34.7	31	9.75
LI-020144	Volcaniclastic basement	42–66 Ma	355/48	C2	7/5	5–80	400–600	53.7	13	53.7	−13	9.9	61.12
				Terable									
LI-020126	Volcaniclastic basement	42–66 Ma	063/23	C2	6/6	25–100	200–580	71.6	3.6	72.1	−19.1	10.6	41.11
LI-020128	Volcaniclastic basement	42–66 Ma	081/27	C2	8/6	≤100	—	30.5	11	31.3	−6.5	1.9	1295
LI-020130	Volcaniclastic basement	42–66 Ma	97/41 (bed) 302/81 (dyke)	C2	7/7	≤70	200–500	55.3	6.5	50.8	−23.7	11.4	28.77

[a]Sites with low temperature/coercivity component with high (k < 15) dispersion.
[b]Poor amygdule orientation. This site was not considered for statistical analysis.
[c]Dip angle may represent depositional slope.
[d]Characteristic direction of site SI-020143 with high dispersion was also excluded for statistical analysis.

uncovered in uppermost Miocene-recent volcanic deposits of El Valle Volcano; these directions are parallel to the Earth's present magnetic field. This northward and shallow positive inclination was also uncovered in two sites of the Mamoni River with low to medium unblocking temperatures (Table 4). The dispersion of directions of the Late component increase after tilt correction (Figures 6g and 7a and Table 5) in the Mamoni sites, supporting an interpretation of a recent magnetization.

[33] Characteristic components uncovered in Oligocene to middle Miocene strata were grouped as the Middle component (B or Br for reversal, in Tables 4 and 5). Although the dispersion of directions of this component decrease after tilt correction (Figures 6h and 7a and Table 5), this result should be considered as preliminary because of (1) the structural complexity in the Canal area, (2) difficulty in calculating the depositional slope in continental volcanics (e.g., Pedro Miguel Formation), and (3) the similarity of some directions with those grouped as the Late component. We interpreted a pre-folding (Oligocene-Middle Miocene) time of magnetization, although more data is necessary to test this hypothesis.

[34] Characteristic components uncovered in volcaniclastic basement rocks north and south of the Rio Gatun Fault and Mamoni-Terable rivers, were grouped as the Early component. This component has negative shallow to intermediate inclinations after tilt correction and show two declination directions (Figures 6i and 7a and Table 5): those rocks with westerly declinations reported in sites north of Rio Gatun Fault (C1 in Tables 4 and 5), and those rocks with northeasterly declinations documented in sites to the south of Rio Gatun Fault and Mamoni-Terable River areas (C2 in Tables 4 and 5).

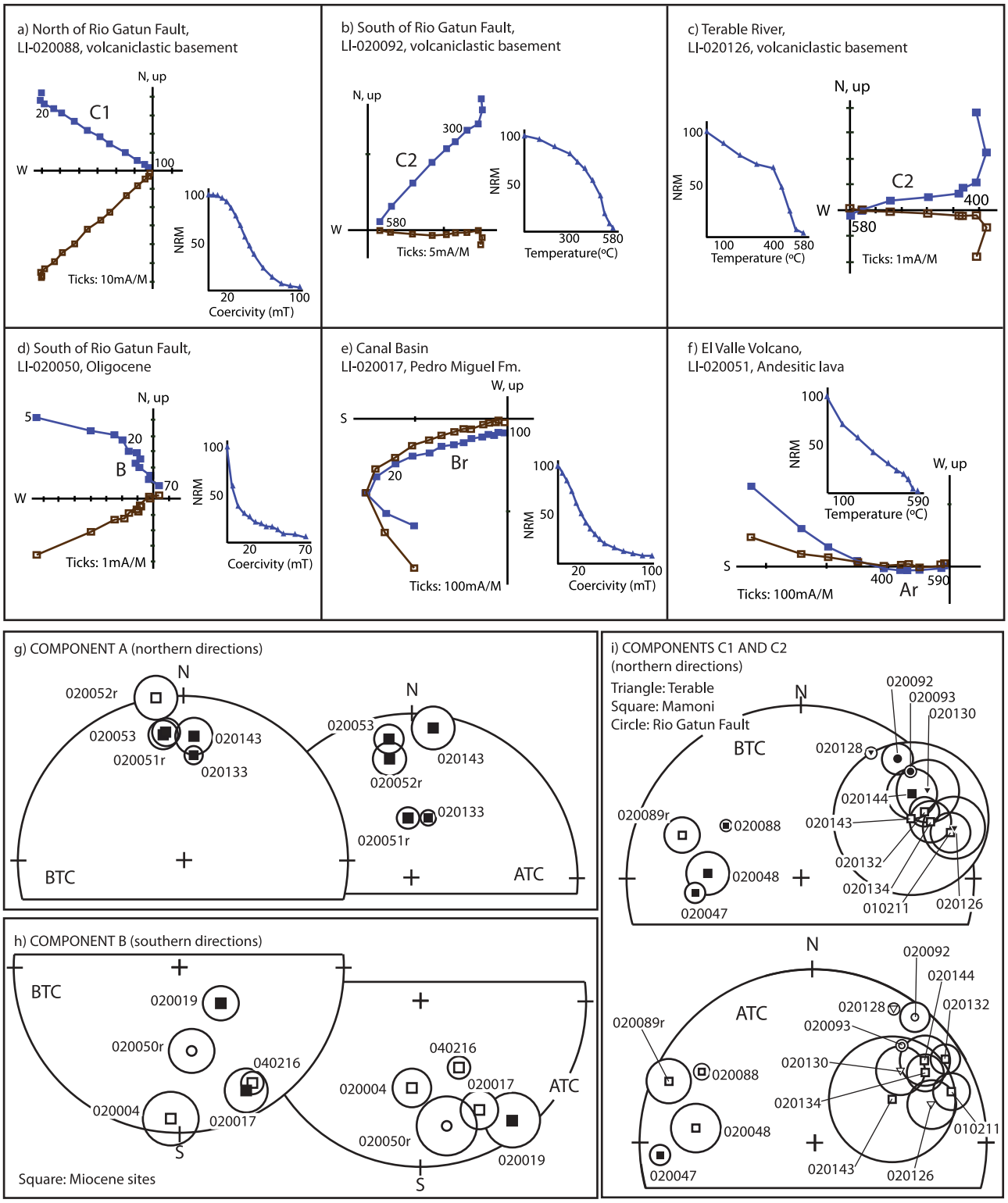

Figure 6. Representative demagnetization diagrams of magnetic components before tilt correction and NRM decay. (a–c) Early components C1 and C2 and (d–f) Late (A) and Middle components (B), r for reversal. Equal-area plots showing site-mean directions grouped as (g) Late component A, (h) Middle component B, and (i) Early components C1 and C2. Open symbols are points in upper hemisphere, closed are lower. See data in Table 1 for sample coordinates.

Table 5. Mean Direction of Components A, B and C (at Specimen Level if N ≤ 3)

		Before Tilt Correction				After Tilt Correction			
Component	N or n	Dec	Inc	a95	k	Dec	Inc	a95	k
A (northern direction)	N = 5	357.2	13.3	10.9	50.1	4.8	20	24.8	10.46
B (southern direction)	N = 5	158.5	1.7	39	4.81	158.5	−20.7	23.6	11.47
C1 north of Rio Gatun Fault (N = 3)	n = 26	288.7	17	11.5	7.09	289.1	−13.8	6.5	19.97
C2 south of Rio Gatun Fault (N = 2)	n = 18	42.3	5.9	3.3	110.14	40	−9.1	4	75.35
C2 Mamoni,Terable	N = 7	59.2	0.8	13.5	20.94	56.2	−13.9	11.1	30.63
C1, C2 (only inclination)	N = 12	—	5.6	9	24.13	—	−12.9	3.3	150.27

[35] Several lines of evidence indicate a near depositional age of magnetization for the Early component. First, well-bedded ocean-floor strata of sites LI-020048 and LI-020089 (Figure 3 and Table 4) record dual polarity magnetization components, suggesting that magnetization might have occurred near deposition. Second, because of differences in declinations, incremental inclination-only tilt test allows accounting for the statistically significant clustering of inclinations at different steps of unfolding in sites north and south of Rio Gatun Fault and Mamoni-Terable areas. The results show a better grouping after tilt correction (Figure 7b), indicating a pre-folding age of magnetization. Third, paleomagnetic components of the volcaniclastic basement complex rocks are markedly different from the Middle and Late components, uncovered in the Oligocene and Middle Miocene volcano-sedimentary cover strata, as well as in the uppermost Miocene to recent volcaniclastic units. On the other hand, comparison of the Early component with directions uncovered in Upper Cretaceous rocks in the Azuero Peninsula [*Di Marco et al.*, 1995], shows similar values of declination. Easterly declinations in Azuero (100° and 103°, Table 6) and very shallow inclinations (0.9° and 3.2°), may be considered as reverse directions of the Early component, similar to the directions uncovered in site LI-020089 (Table 4).

6. Discussion

[36] Determining the timing and mode of deformation of the Isthmus can be done using a combination of two independent constraints: 1) a geometric constraint, where the occurrence of a segmented basement complex represents a strain marker; and 2) a kinematic constraint, where paleomagnetic declination data reveal contrasting, but consistent, vertical-axis rotations on either side of the Rio Gatun Fault. We integrate new and published geochronological data from intermediate intrusive rocks, as well as geochemical data from a plateau to arc volcaniclastic succession to highlight the homogeneity of the basement complex throughout the Isthmus (Figure 8). We also integrate new and published paleomagnetic declination values uncovered in the same arc- and plateau-related basalts. The combination of a regional-scale strain marker and paleomagnetic data are used to perform a restoration of the arc (Figure 9).

6.1. Geometric Constraints

[37] Any feature that is found displaced or deformed, may constitute a strain marker useful for geometric reconstructions. We geochronologically and geochemically fingerprinted a segmented belt of intermediate plutonic rocks intruding a volcaniclastic succession in the Isthmus of Panama (here called the Campanian to Eocene belt), in order to establish former continuity [*Recchi and Metti*, 1975; *Lissina*, 2005]. We review below these geochronological and geochemical data.

6.1.1. Campanian to Eocene Belt in the Azuero Peninsula

[38] In south Costa Rica and west Panama (segment 1 on Figure 3), the western part of the Campanian to Eocene belt is exposed in the outermost fore-arc and includes the Golfito Complex and Azuero Marginal Complex [*Buchs et al.*, 2010], also described as the "Sona-Azuero Arc" in west Panama [*Wegner et al.*, 2011]. The Azuero Marginal Complex has been interpreted as a lateral equivalent of the Golfito Complex [*Buchs et al.*, 2010]. It is composed of massive and pillow lavas with scarce radiolarites of Coniacian-early Santonian age, covered or interbedded with Campanian-Maastrichtian hemipelagic limestone with a local tuffaceous component. These are crosscut by mafic dykes and covered by silicic lavas and related intermediate intrusives of proto-arc to arc sequences [*Buchs et al.*, 2010]. These volcanic sequences have been tectonostratigraphically subdivided into the Azuero Plateau, Azuero Proto-arc Group and Azuero Arc Group, which document a geochemical transition from oceanic plateau to arc magmatism (see detailed description by *Buchs et al.* [2010]).

[39] Intermediate plutonic rocks intruding the Azuero Plateau, Azuero Proto-arc and Azuero Arc Group, yield U/Pb zircon crystallization ages between 67.6 ± 0.4 and 41.1 ± 0.7 Ma (Figure 2), overlapping with published K/Ar and Ar/Ar ages ranging between 69 and 49 Ma [*Guidice and Recchi*, 1969; *Kesler et al.*, 1977; *Lissina*, 2005]. Magmatic products of the same age have also been inferred from magmatic contents preserved in the volcanic-sedimentary sequences of the fore-arc and back-arc basins of Costa Rica [*de Boer et al.*, 1995]. Additionally, effusive rocks in Azuero have also yielded Ar/Ar ages between 67.4 ± 1.9 and 71.1 ± 2 Ma [*Wegner et al.*, 2011].

6.1.2. Campanian to Eocene Belt in the San Blas Range

[40] The eastern part of the Campanian to Eocene belt in the San Blas Range along the Terable, Mamoni and Charare riverbeds (Figure 3) has been described as a ~3 km-thick, folded and faulted sequence, intruded by intermediate plutonic rocks [*Montes et al.*, 2012]. From bottom to top, the volcaniclastic basement sequence is composed of: 1) massive and pillow basalt interlayered with chert and limestone, crosscut by diabase dikes; 2) massive basalt, pillow basalt, diabase, and basaltic dikes and inter-layered pelagic sedimentary rocks; and 3) basaltic andesite lava flows and tuffs. Basalts and basaltic andesites yield Ar/Ar ages between 65.8 ± 2.8 and 41.5 ± 2 Ma [*Wegner et al.*, 2011].

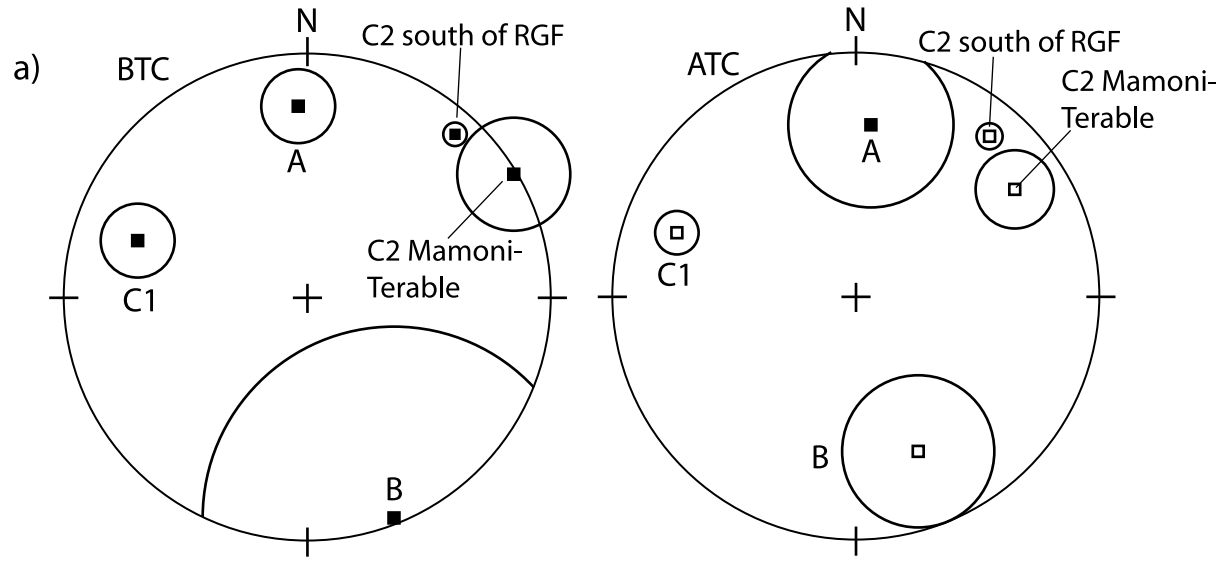

b) Tilt test of Component C1 north of RGF (except site LI-020047)

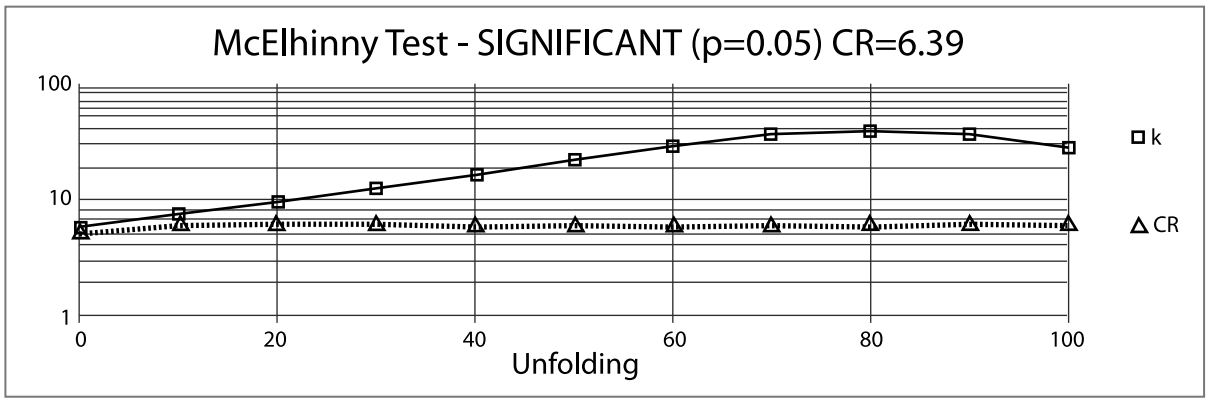

Tilt test of Component C2 in Mamoni area (except site LI-020143)

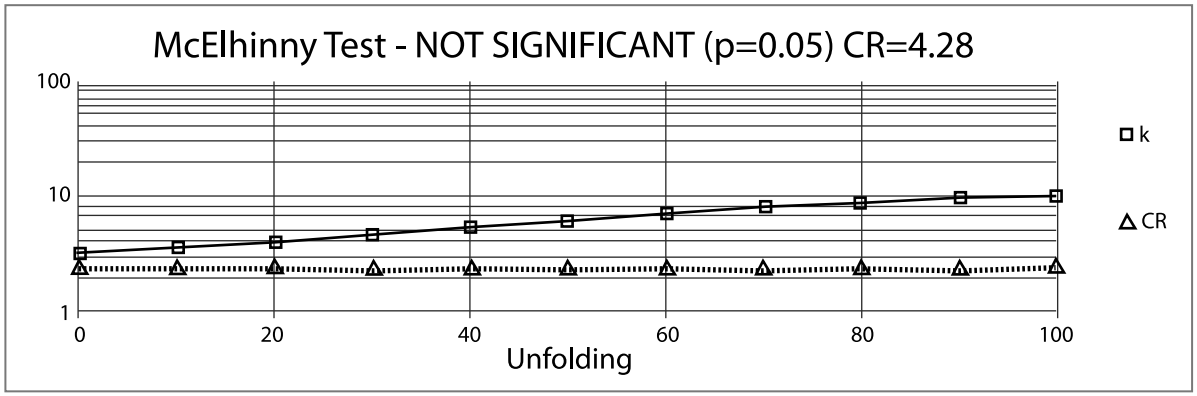

Figure 7. (a) Equal-area plots showing component-mean directions. Inclinations are all positive before tilt correction, Middle (B), and Early (C1 and C2) components becoming negative after correction. Better grouping is shown after tilt correction except for the Late component (A). Sites LI-020047 (C1) and LI-020143 (C2) were not used to calculate the mean direction due to poor bedding control and high dispersion, respectively. (b) Results of local incremental inclination-only test for the Early components (C1 and C2). These diagrams plot k (squares, an estimate of the degree of clustering of inclination data on a sphere) and CR (triangles, a critical ratio above which k values become significant at the 95% confidence level) versus percent of unfolding. RGF: Rio Gatun Fault.

Table 6. Paleomagnetic Directions Reported by *Di Marco et al.* [1995]

			Before Tilt Correction				After Tilt Correction			
Site	Age	N	Dec	Inc	a95	k	Dec	Inc	a95	k
			Changuinola (Chorotega Terrane)							
20	Camp./Maast.	12	162.7	3.8	3.3	179.1	161.9	−7.7	3.2	190.4
21	Camp./Maast.	11	341.3	11.5	8.8	28.1	339.8	14.1	8.7	28.2
			Azuero (Golfito Terrane)							
22	Upper Cretaceous	11	97.4	13.1	6.0	58.3	100.1	0.9	6.0	58.1
23	Upper Cretaceous	7	99.3	33.5	9.6	40.6	103.3	3.2	8.0	58.1

Granitoids intruding the volcaniclastic basement yield ages between 66.4 ± 3.2 Ma and 39.4 ± 0.8 Ma [*Wegner et al.*, 2011; *Montes et al.*, 2012]. In the eastern part of the San Blas Range (Rio Morti area), clasts of basalts to rhyolites yield K/Ar ages between 60.8 ± 1.3 and 55.2 ± 1.2 Ma [*Maury et al.*, 1995].

[41] Stratigraphic constraints [*Montes et al.*, 2012] and our geochemical results document the existence of oceanic plateau rocks overlain by protoarc to arc sequences in the San Blas Range (Figures 4 and 5). Although the presence of oceanic plateau rocks is documented here, their regional continuity or prevalence in low stratigraphic positions could not be established. The stratigraphically lower igneous rocks (Group I), are interpreted as the uppermost layers of a Late Cretaceous oceanic plateau that forms the basement of the south Central American arc. Trace element patterns of Group I, in a PM-normalized multielement diagram, lack negative Nb-Ta or Ti anomalies generally observed in supra-subduction magmas, and TiO2 contents of Group I are lower than those of MORB or typical ocean island basalts.

[42] Stratigraphically above the oceanic plateau rocks, igneous rocks are classified as protoarc sequences (Group II). Geochemical affinities of this group are similar to oceanic plateau signatures with various Th and LREE enrichment/depletion, and small Nb-Ta, Zr-Hf and Ti negative anomalies on a primitive mantle-normalized multielement diagram. However, trace element contents and geochemical trends of Group II are broadly intermediate between those of the oceanic plateau at the base of the arc (i.e., Group I and Azuero Plateau), and those of the more mature South Central American Arc (i.e., Group III, Azuero Arc Group and Morti River igneous rocks, see below).

[43] Stratigraphically higher, most samples of the Chagres Basin formerly described as the Upper Chagres River basin [*Wörner et al.*, 2005], Early Arc [*Wörner et al.*, 2009] or Chagres-Bayano Arc [*Wegner et al.*, 2011], are interpreted by these previous authors as a volcanic arc (Group III). Rocks of this group were mapped as the uppermost part of the volcaniclastic basement, preserved on the axis of synclinal folds [*Montes et al.*, 2012]. As formerly pointed out [*Wörner et al.*, 2005, 2009], strong depletion of Nb-Ta contents relative to Th and rare earth elements in Group III are evidence for a supra-subduction origin.

6.2. The Campanian to Eocene Belt as a Strain Marker

[44] Along-strike similarities from southern Costa Rica to western Colombia that define the Late Campanian to Eocene belt include geochemical fingerprint, granitoid crystallization ages, as well as sedimentation styles and ages. The three distinctive geochemical groups (from I to III), represent a succession from oceanic plateau to supra-subduction arc that stretches from the Azuero Peninsula to the eastern San Blas Range (Figures 4 and 5). Intermediate plutonic rocks of Campanian to Eocene ages intrude these successions underscore their homogeneity (Figures 2 and 8). Highlighting the homogeneity of this succession, upper Eocene to Oligocene, sub-aerial to shallow marine strata of the Tonosi and Gatuncillo formations, and other unnamed strata, unconformably overly both basaltic and intermediate plutonic rocks throughout Panama [*Woodring*, 1957; *Lissina*, 2005; *Buchs et al.*, 2011b; *Montes et al.*, 2012].

[45] Stratigraphic relationships of Group II with Groups I and III in the studied area (Figures 4 and 5) resemble those observed between the Azuero Plateau, protoarc and arc sequences in south Costa Rica and west Panama [*Buchs et al.*, 2010], suggesting broadly similar development of the margin from south Costa Rica to central Panama in the Late Cretaceous-Early Cenozoic. Coeval emplacement of arc-related igneous rocks in the Rio Morti area [*Maury et al.*, 1995], central Panama [*Wörner et al.*, 2005, 2009; *Wegner et al.*, 2011; this study], and Azuero Peninsula [*Lissina*, 2005; *Wörner et al.*, 2009; *Buchs et al.*, 2010; *Wegner et al.*, 2011] define a volcanic front in southern Central America in the Latest Cretaceous and Paleogene. We emphasize here that along-strike similarities along the arc are not limited to magmatic-stratigraphic constraints, but also include granitoid crystallization ages (Figure 8), as well as upper Eocene to Oligocene strata. We therefore suggest that this now segmented belt was an originally continuous and contiguous, supra-subduction magmatic belt built on older Caribbean Plateau rocks during Campanian to Eocene times that can be used as a strain marker (Figure 9a) useful for paleogeographic reconstructions. We include in this belt the ranges of the Mande Batholith in western Colombia (Segment 3, Figure 1), where reconnaissance sampling and mapping show the nearly 400 km-long Mande Batholith made of intermediate plutonic rocks, with K/Ar crystallization ages between 54.7 ± 1.3 and 42.7 ± 0.9 Ma [*Sillitoe et al.*, 1982; *Aspden et al.*, 1987], and middle Eocene cooling ages [*Villagomez*, 2010] similar to those reported in the San Blas Range [*Montes et al.*, 2012].

6.3. Kinematic Constraints

[46] Paleomagnetic declination data uncovered in rocks of the San Blas Range within arc sequences (mostly Group III) record clockwise vertical-axis block rotations southeast of Rio Gatun Fault, and opposite counterclockwise block rotations north and west of the fault (Figure 9a). Additional to the paleomagnetic sites reported here (Table 4), we use *Di Marco et al.*'s [1995] declination data from sites in Chorotega and Azuero (sites 20 to 23, Table 6).

[47] The Early components (C1 and C2 in Figure 7a) reveal moderate to large vertical-axis block rotations with respect to a reference declination and with opposite sense of rotation across the Rio Gatun Fault. We used the geographic north (0° N) as the reference declination, assuming that the present geomagnetic pole is located at the geographic north pole. The magnitude of counterclockwise block rotation defined by westerly declinations north of the Rio Gatun

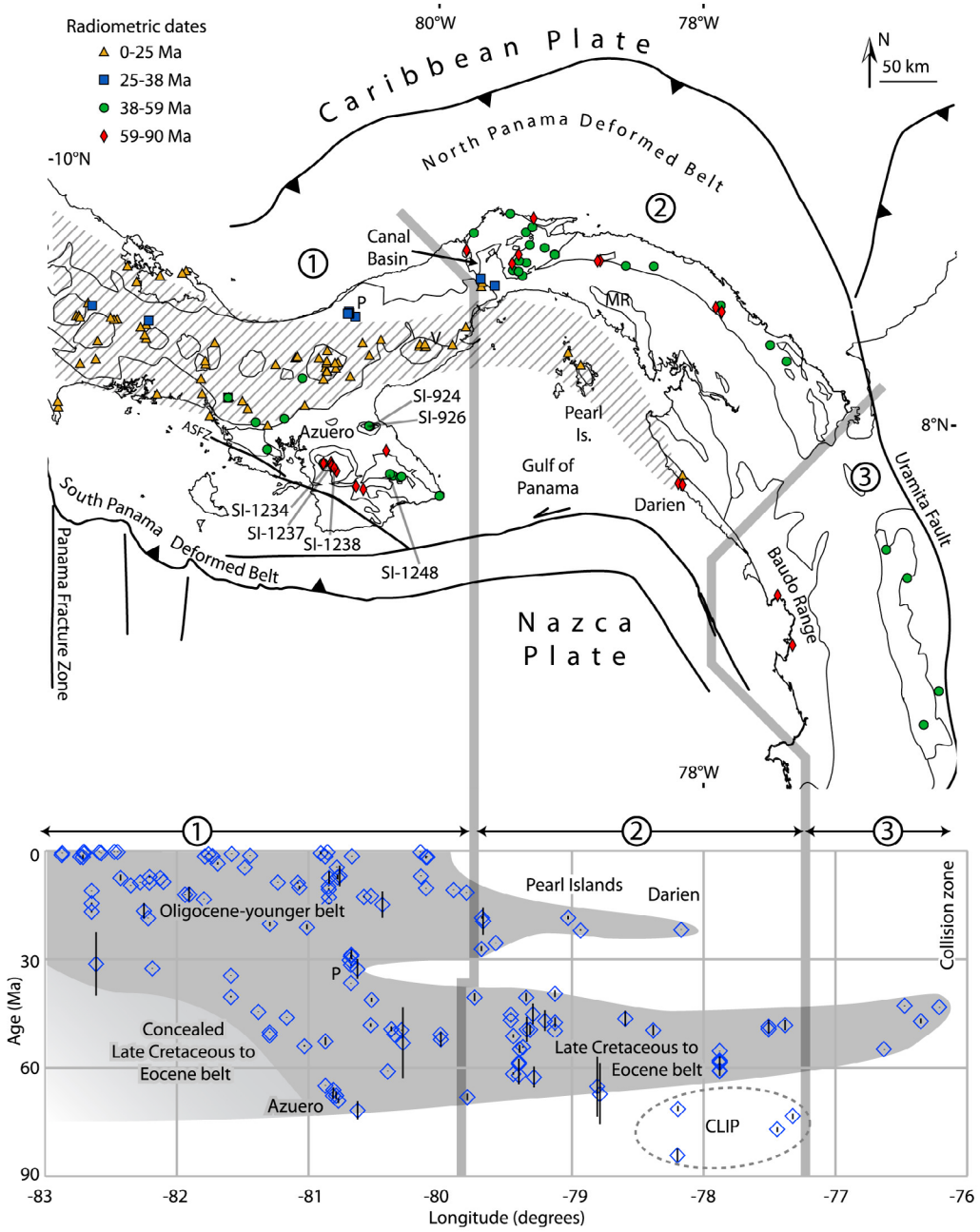

Figure 8. (top) Geographic and (bottom) age distributions of radiometric ages available in the Isthmus of Panama and western Colombia. Radiometric ages, orthogonally projected on an east-west section, reveal nearly continuous magmatic activity in the Chorotega block, a cessation of magmatism at 38 Ma in the San Blas Range, and renewed Oligocene to Miocene activity (diagonal pattern in map) along the Central American arc and south of the San Blas Range. This geometric arrangement constrains the age of left-lateral offset to be younger than 38 Ma, and older than 28 Ma.

Fault is 70.9° ± 6.7° that may increase to ~80° if Azuero declinations are considered (Table 6). The magnitude of clockwise block rotation defined by northeasterly declinations south of Rio Gatun Fault is 40° ± 4.1°. Farther east, the Mamoni-Terable area also shows clockwise block rotations of 56.2° ± 11.1° with respect to the geographic north, and 16.2° ± 12.1° with respect to the southern block of the Rio Gatun Fault (Table 5). Although additional sites are required to validate the Middle component (B in Table 4), due to the structural complexities in the sampling areas, it suggests some block rotation (21.5° ± 23.6°, Table 5), where 3 of 5 sites suggest significant rotations at 95% confidence (Figure 6). The Late component records no significant block rotations (Figure 7a). Upper Cretaceous-Eocene rocks, the oldest rocks in the region, record all the finite rotation uncovered in the region. Younger rocks, such as the

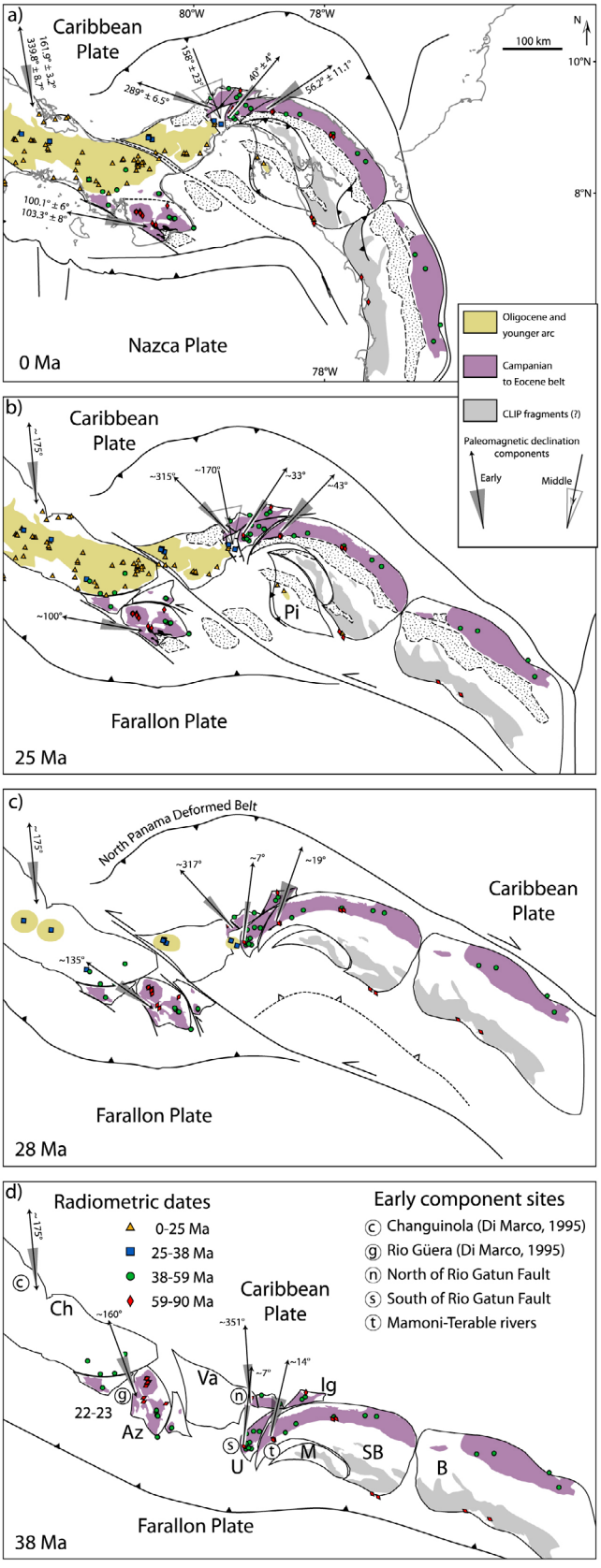

Oligocene-Miocene rocks record only an increment of this rotation. The most significant vertical axis rotations took place after middle Eocene times (Early components, Figure 9d, ~38 Ma), but before Oligocene-early Miocene times (Middle component, ~28–25 Ma, Figures 9c and 9b). An increment of vertical-axis rotation took place in middle Miocene times, and no rotations took place since then (Late component, Figure 9a).

6.4. Chronology and Style of Isthmus Deformation

[48] From these data we reconstructed the chronology and style of deformation in the Isthmus of Panama (Figure 9). We used the Campanian to Eocene belt as the primary strain marker, and the overlapping, Central American arc —continuous and linear— as the arc that seals the age of deformation [*Recchi and Metti*, 1975; *Defant et al.*, 1991a, 1991b; *Coates and Obando*, 1996; *MacMillan et al.*, 2004; *Lissina*, 2005; *Hidalgo et al.*, 2011]. Paleomagnetic data suggest a style of deformation consistent with a secondary orocline [*Weil and Sussman*, 2004], as the geometry of the belt was modified by vertical-axis rotation and strike-slip faulting. It differs from the original orocline definition, in that the original arc is defined by a regional magmatic fabric (Figure 8), not a deformational one. This reconstruction contrasts with the simple bending model of *Silver et al.* [1990], in that discrete faults accommodate internal deformation in the Isthmus. It is more akin to the distributed left-lateral shear model of *Mann and Corrigan* [1990], but incorporates the vertical-axis rotation of blocks, pushes the age of deformation back to middle Eocene to early Oligocene, and uses faults of many different orientations, not only northwest-trending.

6.5. Tectonic Blocks Used in Reconstruction

[49] Tectonic block boundaries for the reconstruction (Figure 9) were defined according to geologic map patterns (Figure 1). In the Azuero Peninsula, the Azuero block is separated from the stable Chorotega block (Chorotega Terrane [*Di Marco et al.*, 1995; *Buchs et al.*, 2010]) by the east-west trending Ocu fault [*Recchi and Metti*, 1975]. The El Valle block is bound by the inferred, northwest-trending, deep shear zones of *Case* [1974] and *Lowrie et al.* [1982], and includes the Isla Grande block (Figure 9), bound to the south by the Rio Gatun Fault (Figure 1) and the Canal Basin faults [*Woodring*, 1957]. In the San Blas Range, the Rio Indio Fault (Figure 3) separates the Utive-Cerro Azul block from San Blas-Darien block to the east. The Unguia Fault (Figure 1) separates the San Blas Range from the Mande

Figure 9. Tectonic reconstruction of the Campanian to Eocene belt. Paleomagnetic components reported in this paper and in the Chorotega terrane and Azuero (sites 20 to 23 of *Di Marco et al.* [1995]) are shown as arrows. The triangle under the arrow defines a mean paleomagnetic declination and its 95% confidence limit. (a) Present configuration, (b) reconstruction at 25 Ma, (c) reconstruction at 28 Ma, and (d) reconstruction at 38 Ma. Az: Azuero-Chorotega block; B: Choco block; Ig: Isla Grande block; M: Maje block; Pi: Perlas block; SB: San Blas-Darien block; U: Utive-Cerro Azul block; Va: El Valle block (mostly covered by Neogene volcanics).

Batholith ranges [*Mann and Corrigan*, 1990; *Mann and Kolarsky*, 1995], while a deformed belt along the northern flank of the Maje Range [*United Nations*, 1972] constitutes the southern boundary of the San Blas-Darien block. The Uramita Fault bounds the Mande Batholith to the east [*Duque-Caro*, 1990a; *Trenkamp et al.*, 2002]. The Perlas block is defined according to tectonic boundaries mapped by *Mann and Kolarsky* [1995]. The northern Panama deformed belt [*Silver et al.*, 1990] marks the northern extent of blocks along the Caribbean edge of Panama (Figure 1).

[50] In this reconstruction, rigid blocks bounded by discrete fault zones, accommodate deformation with structures trending in very different orientations: nearly north-south along the Canal Basin, northeast trending in the Utive-Cerro Azul block, east-west trending in the Maje Range, and nearly north-south further east in the Chucunaque Basin (Figure 1). Changes in the magnitudes of vertical-axis rotations across blocks are solved by left-lateral strike-slip faulting (Rio Indio Fault), extensional deformation (Canal Basin blocks), or shortening and dextral, north-south faulting (southern end of Chucunaque Basin and western Perlas block).

6.6. Reconstruction

[51] Tectonic blocks above defined were used to perform a simple restoration in plan view to bring the Campanian to Eocene belt to a continuous configuration according to paleomagnetic declination data (Figure 9d). Rotation of blocks according to their paleomagnetic declination data (Early C1 and C2 components), including published declination data of *Di Marco et al.* [1995], was performed to achieve a near north-declinations, yielding as a result, a near-linear Campanian to Eocene magmatic belt. Failure to reach north-south declinations by about 5° to 20° in the initial stage of the model (Figure 9d) may represent original arc curvature (opposite to today's curvature), or internal deformation within the blocks not considered in this reconstruction. Failure to reach north-south declinations after the Campanian to Eocene belt achieves a near-linear configuration, however, is within the 95% confidence limit for most of the paleomagnetic declinations.

[52] A summary of the events and the chronology of deformation is as follows. After 38 Ma, but before the restart of the arc at 28 Ma, a large (~100 km), left-lateral, northwestward fault displaces the El Valle and Azuero blocks; this is accompanied by large counterclockwise vertical-axis rotations in the Azuero Peninsula (20°) and El Valle block (34°), and small (0 to 5°) clockwise rotations in the Utive and San Blas blocks (Figure 9c). Between 28 and 25 Ma the Utive and San Blas blocks accrue most of the clockwise vertical-axis rotation (26° and 24° respectively, Early component, Figures 9c and 9b). After most, but not all, of these vertical-axis rotations are completed, an Oligocene and younger arc crosscuts the already offset Campanian to Eocene belt, tracing an originally gentle curvilinear path (Figure 9b) that becomes tighter due to late deformation (Figure 9a), as recorded by the Middle paleomagnetic component (component B). The Late paleomagnetic component (component A) shows no significant vertical-axis rotation (Figures 6 and 7) and further constrains this age of deformation.

[53] The north-south trending Choco block (segment 3 in Figure 1), now docked to western South America, is assumed in this reconstruction to follow a geometric configuration approximately along the strike of segments 1 and 2 of the Campanian to Eocene belt in the restored state (Figure 9d). This assumption is supported by: 1) Late Cretaceous ages [*Lissina*, 2005] and geochemical character of the volcaniclastic basement [*Kerr et al.*, 1997b] similar to ages and geochemical characteristics above discussed for the volcaniclastic basement of the San Blas Range and the plateau rocks of the Azuero Peninsula; 2) the similarities between the Chucunaque Basin (Figure 1) in segment 2, and the Atrato Basin in segment 3 of the Isthmus [*Case*, 1974; *Duque-Caro*, 1990a, 1990b; *Kellogg and Vega*, 1995; *Trenkamp et al.*, 2002; *Coates et al.*, 2004]; and 3) crystallization [*Sillitoe et al.*, 1982; *Aspden et al.*, 1987] and cooling [*Villagomez*, 2010] ages of the Mande Batholith (Figure 1), similar to those reported in the San Blas Range [*Farris et al.*, 2011; *Wegner et al.*, 2011; *Montes et al.*, 2012]. Although we performed pilot sampling and demagnetization from rocks in this belt, no paleomagnetic components could be isolated.

[54] From this reconstruction, it follows that the S shape of the Isthmus may have been achieved by oroclinal bending where discrete faults separated relatively rigid blocks that rotated around vertical axes (Figure 9). Left-lateral offset of the Campanian to Eocene belt between 38 and 28 Ma, opening of the Canal Basin at ~25 Ma [*Farris et al.*, 2011], and initiation of the North Panama Deformed Belt [*Silver et al.*, 1990], as the Panama-Choco Block was thrust to the northwest on to the Caribbean Plate [*Kellogg and Vega*, 1995; *Camacho et al.*, 2010] are all result of oroclinal bending of the arc. The late Oligocene (~25 Ma) deformation may represent the early stages of collision with South America [*Farris et al.*, 2011].

[55] This restored belt (Figure 9) can now be placed in a paleogeographic space (Figure 10), where the gap between North and South America is constrained using mid-Atlantic ocean-floor anomalies (using Gplates software) [*Boyden et al.*, 2011; *Gurnis et al.*, 2012]. Additional constraints include: 1) a necessary early to middle Miocene land connection between North America and the Canal Basin [*Kirby and MacFadden*, 2005]; 2) the shape of the restored northwestern South American margin [*Pindell*, 1993; *Montes et al.*, 2005; *Pindell and Kennan*, 2009; *Montes et al.*, 2010]; and 3) the linear chain of Central American volcanoes, that seal age of docking of the Central American arc to the Chortis block —and the Chortis block to Yucatan— to be middle Miocene [*MacMillan et al.*, 2004]. Placed in such paleogeographic frame, the gap narrows at about 25 Ma [*Farris et al.*, 2011], and disappears at about 15 Ma (Figure 10). The cause of the late Eocene to early Oligocene (38–28 Ma) deformation is still unclear as the gap is too wide at this time in this reconstruction to allow collision.

[56] Since the Campanian to Eocene belt was exhumed [*Montes et al.*, 2012] by the time the gap disappears at 15 Ma, any significant deep-water circulation through the Central American seaway would be severed since middle Miocene times. These results make it difficult to envision the location of a deep-water passage in the Central American region, and challenges the view that changes in deep water

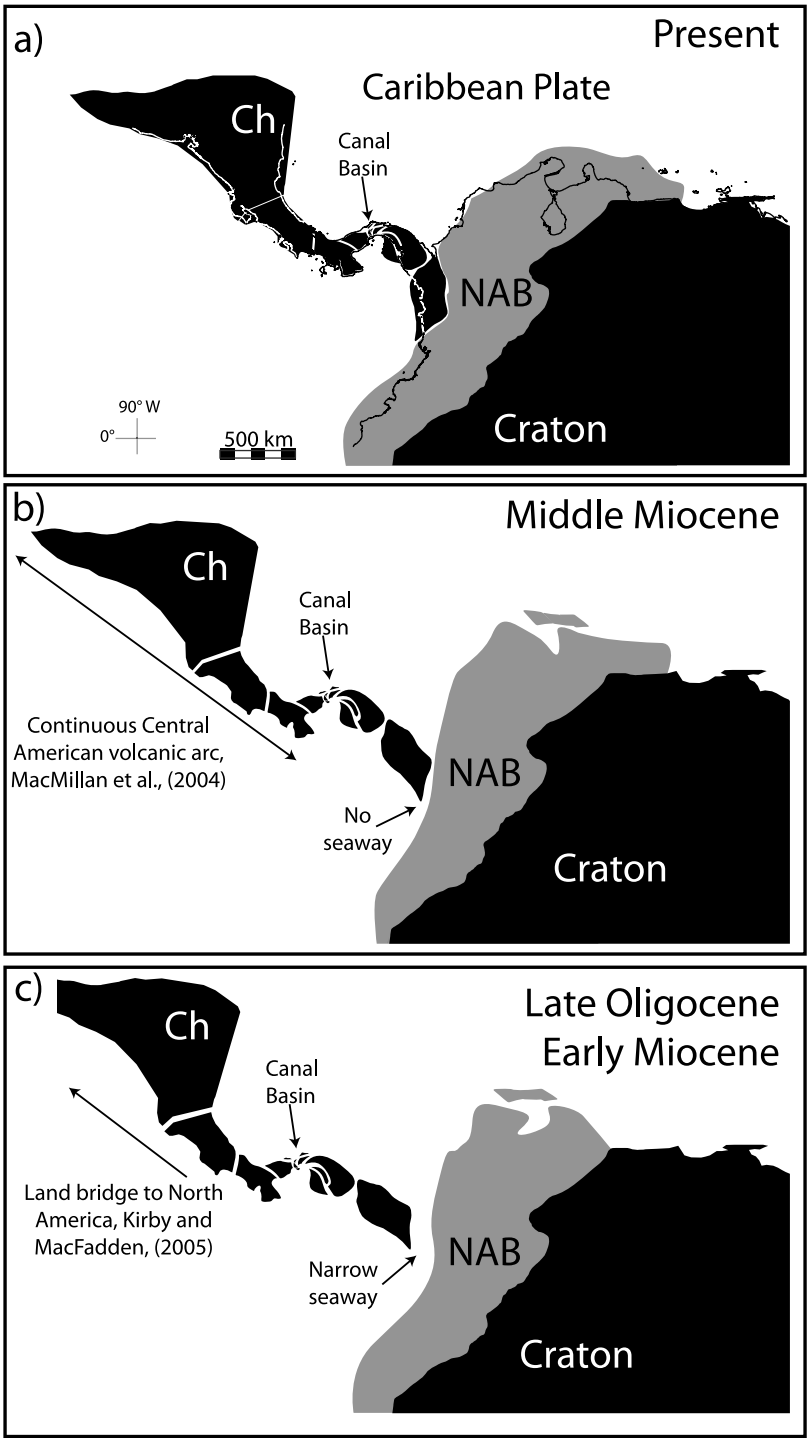

Figure 10. Reconstruction of the Campanian to Eocene belt placed in a global plate tectonic database. The distance between the Chortis block (Ch) and the northern Andean blocks (NAB) is filled with this belt restored at the appropriate time interval (from Figure 9). (a) Present configuration; (b) at the time of seaway closure (middle Miocene), the Campanian to Eocene belt was exhumed [*Montes et al.*, 2012]; and (c) by the late Oligocene to early Miocene, the gap was narrow [*Farris et al.*, 2011]. See text for discussion.

circulation triggered late Piocene climate change [*Haug et al.*, 2001].

7. Conclusions

[57] Four main conclusions can be derived from the data presented in this paper: 1) a geochemically homogeneous succession of plateau to supra-subduction arc rocks, intruded by a similar suite of Campanian to Eocene intermediate plutonic rocks spans the Chorotega, and Panama-Choco blocks and defines a strain marker suitable for tectonic reconstructions; 2) segmentation of this belt started during late Eocene-early Oligocene times (38 to 28 Ma), and was nearly completed by late Oligocene times (∼25 Ma); 3) deformation of this belt was achieved by vertical-axis rotation of rigid blocks with opposite rotation sense on both sides of the Rio Gatun Fault; 4) once this belt is restored and placed in a paleogeographic position, the space for the Central American seaway narrows at ∼25 Ma, and disappears by about 15 Ma. It is therefore likely that significant deep-water circulation across the Central American seaway had been severed well before late Pliocene times.

[58] **Acknowledgments.** Project supported by Panama Canal Authority contract SAA-199520-KRP; Mark Tupper; Senacyt grants SUM-07-001 and EST010–080 A; U.S. National Science Foundation (NSF) grant 0966884 (OISE, EAR, DRL); Colciencias; Swiss National Science Foundation (project PBLA2–122660); NSF EAR 0824299; National Geographic; Smithsonian Institution; and Ricardo Perez S.A. Thanks to J. E. T. Channell, K. Huang, S. Zapata, R. Arculus, C. Allen, A. Christy and U. Troitzsch. Access and collection permits were granted by Panama Canal Authority and Ministerio de Industria y Comercio. We are grateful to all participants of February's 2010 joint workshop IGCP 546 "Subduction Zones of the Caribbean" and 574 "Bending and Bent Orogens, and Continental Ribbons." Thanks to G. Wörner, J. Pindell, S. Johnson, P. Molnar, R. Somoza, and P. Mann for their reviews and comments to our manuscript as it evolved.

References

Adamek, S., C. Frohlich, and D. Pennington Wayne (1988), Seismicity of the Caribbean-Nazca boundary: Constraints on microplate tectonics of the Panama region, *J. Geophys. Res.*, *93*, 2053–2075, doi:10.1029/JB093iB03p02053.

Arculus, R. J. (2003), Use and abuse of the terms calcalkaline and calcalkalic, *J. Petrol.*, *44*(5), 929–935, doi:10.1093/petrology/44.5.929.

Aspden, J. A., W. J. McCourt, and M. Brook (1987), Geometrical control of subduction-related magmatism: The Mesozoic and Cenozoic plutonic history of western Colombia, *J. Geol. Soc.*, *144*, 893–905, doi:10.1144/gsjgs.144.6.0893.

Baumgartner, P. O., K. Flores, A. N. Bandini, F. Girault, and D. Cruz (2008), Upper Triassic to Cretaceous radiolaria from Nicaragua and northern Costa Rica—The Mesquito Composite Oceanic Terrane, *Ofioliti*, *33*(1), 1–19.

Boyden, J., R. D. Müller, M. S. Gurnis, T. Torsvik, J. A. Clark, M. Turner, H. Ivey-Law, R. J. Watson, and J. S. Cannon (2011), Next-generation plate-tectonic reconstructions using GPlates, in *Geoinformatics: Cyberinfrastructure for the Solid Earth Sciences*, edited by G. R. Keller and C. Baru, pp. 95–114, Cambridge Univ. Press, Cambridge, U. K., doi:10.1017/CBO9780511976308.008.

Buchs, D. M., P. O. Baumgartner, C. Baumgartner-Mora, A. N. Bandini, S. J. Jackett, M. O. Diserens, and J. Stucki (2009), Late Cretaceous to Miocene seamount accretion and mélange formation in the Osa and Burica Peninsulas (southern Costa Rica): Episodic growth of a convergent margin, in *The Origin and Evolution of the Caribbean Plate*, edited by H. James Keith, M. A. Lorente, and L. Pindell James, *Geol. Soc. Spec. Publ.*, *328*, 411–456.

Buchs, D. M., R. J. Arculus, P. O. Baumgartner, C. Baumgartner-Mora, and A. Ulianov (2010), Late Cretaceous arc development on the SW margin of the Caribbean Plate: Insights from the Golfito, Costa Rica, and Azuero, Panama, complexes, *Geochem. Geophys. Geosyst.*, *11*, Q07S24, doi:10.1029/2009GC002901.

Buchs, D. M., R. J. Arculus, P. O. Baumgartner, and A. Ulianov (2011a), Oceanic intraplate volcanoes exposed: Example from seamounts accreted in Panama, *Geology*, *39*(4), 335–338, doi:10.1130/G31703.1.

Buchs, D. M., P. O. Baumgartner, C. Baumgartner-Mora, K. Flores, and A. N. Bandini (2011b), Upper Cretaceous to Miocene tectonostratigraphy of the Azuero area (Panama) and the discontinuous accretion and subduction erosion along the Middle American margin, *Tectonophysics*, *512*, 31–46, doi:10.1016/j.tecto.2011.09.010.

Burton, K. W., H.-F. Ling, and R. K. O'Nions (1997), Closure of the Central American Isthmus and its effect on deep-water formation in the North Atlantic, *Nature*, *386*(6623), 382–385, doi:10.1038/386382a0.

Camacho, E., W. Hutton, and J. F. Pacheco (2010), A new look at evidence for a Wadati-Benioff zone and active convergence at the north Panama deformed belt, *Bull. Seismol. Soc. Am.*, *100*(1), 343–348, doi:10.1785/0120090204.

Case, J. E. (1974), Oceanic crust forms basement of eastern Panama, *Geol. Soc. Am. Bull.*, *85*, 645–652, doi:10.1130/0016-7606(1974)85<645:OCFBOE>2.0.CO;2.

Coates, A. G., and J. A. Obando (1996), The geologic evolution of the Central American isthmus, in *Evolution and Environment in Tropical America*, edited by J. B. C. Jackson, A. F. Budd, and A. G. Coates, pp. 21–56, Univ. of Chicago Press, Chicago, Ill.

Coates, A. G., L. S. Collins, M.-P. Aubry, and W. A. Berggren (2004), The geology of the Darien, Panama, and the late Miocene-Pliocene collision of the Panama arc with northwestern South America, *Geol. Soc. Am. Bull.*, *116*(11), 1327–1344, doi:10.1130/B25275.1.

Corfu, F., J. M. Hanchar, P. W. O. Hoskin, and P. Kinny (2003), Atlas of zircon textures, *Rev. Mineral. Geochem.*, *53*, 469–500, doi:10.2113/0530469.

Corral, I., A. Giera, D. Gomez-Gras, M. Corbella, A. Canals, M. Pineda-Falconett, and E. Cardellach (2011), The geology of the Cerro Quema Au-Cu deposit (Azuero Peninsula, Panama), *Geol. Acta*, *9*(3–4), 481–498.

de Boer, J. Z., M. J. Defant, R. H. Stewart, J. F. Restrepo, L. F. Clark, and A. H. Ramirez (1988), Quaternary calc-alkaline volcanism in western Panama: Regional variation implication for the plate tectonic framework, *J. South Am. Earth Sci.*, *1*(3), 275–293, doi:10.1016/0895-9811(88)90006-5.

de Boer, J. Z., M. J. Defant, R. H. Stewart, and H. Bellon (1991), Evidence for active subduction below western Panama, *Geology*, *19*(6), 649–652, doi:10.1130/0091-7613(1991)019<0649:EFASBW>2.3.CO;2.

de Boer, J. Z., S. Drummond Mark, M. J. Bordelon, J. Defant Marc, H. Bellon, and C. Maury Rene (1995), Cenozoic magmatic phases of the Costa Rican island arc (Cordillera de Talamanca), *Spec. Pap. Geol. Soc. Am.*, *295*, 35–55.

Defant, M. J., L. F. Clark, R. H. Stewart, M. S. Drummond, J. Z. de Boer, R. C. Maury, H. Bellon, T. E. Jackson, and J. F. Restrepo (1991a), Andesite and dacite genesis via contrasting processes: The geology and geochemistry of El Valle Volcano, Panama, *Contrib. Mineral. Petrol.*, *106*(3), 309–324, doi:10.1007/BF00324560.

Defant, M. J., P. M. Richerson, J. Z. de Boer, R. H. Stewart, R. C. Maury, H. Bellon, M. S. Drummond, M. D. Feigenson, and T. E. Jackson (1991b), Dacite genesis via both slab melting and differentiation: Petrogenesis of La Yeguada Volcanic Complex, Panama, *J. Petrol.*, *32*(6), 1101–1142.

Demarest, H. (1983), Error analysis for determination of tectonic rotation from paleomagnetic data, *J. Geophys. Res.*, *88*, 4321–4328, doi:10.1029/JB088iB05p04321.

Di Marco, G., P. O. Baumgartner, and J. E. T. Channell (1995), Late Cretaceous-early Tertiary paleomagnetic data and a revised tectonostratigraphic subdivision of Costa Rica and western Panama, in *Geologic and Tectonic Development of the Caribbean Plate Boundary in Southern Central America*, edited by P. Mann, pp. 1–27, Geol. Soc. of Am., Boulder, Colo.

Duque-Caro, H. (1990a), The Choco Block in the northwestern corner of South America: Structural, tectonostratigraphic, and paleogeographic implications, *J. South Am. Earth Sci.*, *3*(1), 71–84, doi:10.1016/0895-9811(90)90019-W.

Duque-Caro, H. (1990b), Neogene stratigraphy, paleoceanography and paleobiogeography in northwest South America and the evolution of the Panama Seaway, *Palaeogeogr. Palaeoclimatol. Palaeoecol.*, *77*(3–4), 203–234, doi:10.1016/0031-0182(90)90178-A.

Farris, D. W., et al. (2011), Fracturing of the Panamanian Isthmus during initial collision with South America, *Geology*, *39*, 1007–1010, doi:10.1130/G32237.1.

Fisher, R. A. (1953), Dispersion on a sphere, *Proc. R. Soc. London, Ser. A*, *217*, 295–305, doi:10.1098/rspa.1953.0064.

Gazel, E., K. Hoernle, M. J. Carr, C. Herzberg, I. Saginor, P. van den Bogaard, F. Hauff, M. D. Feigenson, and C. Swisher (2011), Plume-

subduction interaction in southern Central America: Mantle upwelling and slab melting, *Lithos*, *121*, 117–134, doi:10.1016/j.lithos.2010.10.008.

Gehrels, G., V. Valencia, and A. Pullen (2006), Detrital zircon geochronology by laser-ablation multicollector ICPMS at the Arizona Laserchron Center, *Paleontol. Soc. Pap.*, *12*, 67–76.

Gehrels, G., V. Valencia, and J. Ruiz (2008), Enhanced precision, accuracy, efficiency, and spatial resolution of U-Pb ages by laser ablation–multicollector–inductively coupled plasma–mass spectrometry, *Geochem. Geophys. Geosyst.*, *9*, Q03017, doi:10.1029/2007GC001805.

Guidice, D., and G. Recchi (1969), Geología del area del proyecto minero de Azuero, report, 48 pp., Programa para el desarrollo de las Nac. Unidas, Panama City.

Gurnis, M. S., M. Zahirovic, L. Turner, S. DiCaprio, R. D. Spasojevic, R. D. Müller, J. Boyden, M. Seton, V. C. Manea, and D. J. Bower (2012), Plate tectonic reconstructions with continuously closing plates, *Comput. Geosci.*, *38*, 35–42.

Hauff, F., K. Hoernle, G. Tilton, D. W. Graham, and A. C. Kerr (2000), Large volume recycling of oceanic lithosphere over short time scales: Geochemical constraints from the Caribbean Large Igneous Province, *Earth Planet. Sci. Lett.*, *174*(3–4), 247–263, doi:10.1016/S0012-821X(99)00272-1.

Haug, G. H., R. Tiedemann, R. Zahn, and A. C. Ravelo (2001), Role of Panama uplift on oceanic freshwater balance, *Geology*, *29*, 207–210, doi:10.1130/0091-7613(2001)029<0207:ROPUOO>2.0.CO;2.

Hawkesworth, C., R. George, S. Turner, and G. Zellmer (2004), Timescales of magmatic processes, *Earth Planet. Sci. Lett.*, *218*, 1–16, doi:10.1016/S0012-821X(03)00634-4.

Hidalgo, P., T. Vogel, T. Rooney, R. Currier, and P. Layer (2011), Origin of silicic volcanism in the Panamanian arc: Evidence for a two-stage fractionation process at El Valle volcano, *Contrib. Mineral. Petrol.*, *162*(6), 1115–1138, doi:10.1007/s00410-011-0643-2.

Hoernle, K., P. van den Bogaard, R. Werner, B. Lissinna, F. Hauff, G. Alvarado, and D. Garbe-Schanberg (2002), Missing history (16–71 Ma) of the Galapagos hotspot: Implications for the tectonic and biological evolution of the Americas, *Geology*, *30*(9), 795–798, doi:10.1130/0091-7613(2002)030<0795:MHMOTG>2.0.CO;2.

Hoernle, K., F. Hauff, and P. van den Bogaard (2004), 70 m.y. history (139–69 Ma) for the Caribbean large igneous province, *Geology*, *32*(8), 697–700, doi:10.1130/G20574.1.

Hoernle, K., et al. (2008), Arc-parallel flow in the mantle wedge beneath Costa Rica and Nicaragua, *Nature*, *451*(7182), 1094–1097, doi:10.1038/nature06550.

Hoskin, P. W. O., and U. Schaltegger (2003), The composition of zircon and igneous and metamorphic petrogenesis, in *Zircon*, edited by J. M. Hanchar and P. W. O. Hoskin, pp. 27–62, Mineral. Soc. of Am., Washington, D. C.

Jackson, J. B. C., P. Jung, A. G. Coates, and L. S. Collins (1993), Diversity and extinction of tropical American mollusks and emergence of the Isthmus of Panama, *Science*, *260*(5114), 1624–1626.

Jordan, T. H. (1975), The present-day motions of the Caribbean plate, *J. Geophys. Res.*, *80*, 4433–4439, doi:10.1029/JB080i032p04433.

Kellogg, J. N., and V. Vega (1995), Tectonic development of Panama, Costa Rica, and the Colombian Andes: Constraints from Global Positioning System geodetic studies and gravity, *Spec. Pap. Geol. Soc. Am.*, *295*, 75–90.

Kennan, L., and J. L. Pindell (2009), Dextral shear, terrane accretion and basin formation in the northern Andes: Best explained by interaction with a Pacific-derived Caribbean Plate?, in *The Origin and Evolution of the Caribbean Plate*, edited by K. H. James, M. A. Lorente, and J. L. Pindell, *Geol. Soc. Spec. Publ.*, *328*, 487–531.

Kerr, A. C., J. Tarney, G. F. Marriner, A. Nivia, and A. D. Saunders (1997a), The Caribbean-Colombian cretaceous igneous province: The internal anatomy of an oceanic plateau, in *Large Igneous Provinces: Continental, Oceanic, and Planetary Flood Volcanism*, *Geophys. Monogr. Ser.*, vol. 100, edited by J. Mahoney and F. Coffin, pp. 123–144, AGU, Washington, D. C., doi:10.1029/GM100p0123.

Kerr, A. C., G. F. Marriner, J. Tarney, A. Nivia, A. D. Saunders, M. F. Thirlwall, and C. W. Sinton (1997b), Cretaceous basaltic terranes in western Colombia: Elemental, chronological and Sr-Nd isotopic constraints on petrogenesis, *J. Petrol.*, *38*(6), 677–702, doi:10.1093/petrology/38.6.677.

Kesler, S. E., J. F. Sutter, M. J. Issigonis, L. M. Jones, and R. L. Walker (1977), Evolution of porphyry copper mineralization in an oceanic island arc: Panama, *Econ. Geol.*, *72*, 1142–1153, doi:10.2113/gsecongeo.72.6.1142.

Kirby, M. X., and B. MacFadden (2005), Was southern Central America an archipelago or a peninsula in the middle Miocene? A test using land-mammal body size, *Palaeogeogr. Palaeoclimatol. Palaeoecol.*, *228*(3–4), 193–202, doi:10.1016/j.palaeo.2005.06.002.

Kirschvink, J. (1980), The least-squares line plane and the analysis of paleomagnetic data, *Geophys. J. R. Astron. Soc.*, *62*, 699–718, doi:10.1111/j.1365-246X.1980.tb02601.x.

Kolarsky, R. A., and P. Mann (1995), Structure and neotectonics of an oblique-subduction margin, southwestern Panama, in *Geologic and Tectonic Development of the Caribbean Plate Boundary in Southern Central America*, edited by P. Mann, *Spec. Pap. Geol. Soc. Am.*, *295*, 131–157.

Kolarsky, R. A., P. Mann, and S. Monechi (1995), Stratigraphic development of southwestern Panama as determined from integration of marine seismic data and onshore geology, in *Geologic and Tectonic Development of the Caribbean Plate Boundary in Southern Central America*, edited by P. Mann, pp. 159–200, Geol. Soc. of Am., Boulder, Colo.

Lear, C. H., Y. Rosenthal, and D. Wright James (2003), The closing of a seaway: Ocean water masses and global climate change, *Earth Planet. Sci. Lett.*, *210*, 425–436, doi:10.1016/S0012-821X(03)00164-X.

Lissina, B. (2005), A profile through the Central American landbridge in western Panama: 115 Ma interplay between the Galápagos hotspot and the Central American subduction zone, doctoral thesis, 102 pp., Christian-Albrechts Univ., Kiel, Germany.

Lowrie, A., J. L. Stewart, R. H. Stewart, T. J. Van Andel, and L. McRaney (1982), Location of the eastern boundary of the Cocos plate during the Miocene, *Mar. Geol.*, *45*(3–4), 261–279, doi:10.1016/0025-3227(82)90114-1.

Ludwig, K. J. (2007), *Isoplot 3.62*, 70 pp., Berkeley Geochonol. Cent., Berkeley, Calif.

MacMillan, I., P. B. Gans, and G. Alvarado (2004), Middle Miocene to present plate tectonic history of the southern Central American Volcanic Arc, *Tectonophysics*, *392*(1–4), 325–348, doi:10.1016/j.tecto.2004.04.014.

Mann, P., and J. Corrigan (1990), Model for late Neogene deformation in Panama, *Geology*, *18*(6), 558–562, doi:10.1130/0091-7613(1990)018<0558:MFLNDI>2.3.CO;2.

Mann, P., and R. A. Kolarsky (1995), East Panama Deformed Belt: Structure, age, and neotectonic significance, in *Geologic and Tectonic Development of the Caribbean Plate Boundary in Southern Central America*, edited by P. Mann, pp. 111–130, Geol. Soc. of Am., Boulder, Colo.

Marshall, L. G., S. D. Webb, J. J. Sepkoski, and D. M. Raup (1982), Mammalian evolution and the Great American Interchange, *Science*, *215*(4538), 1351–1357.

Maury, R. C., M. J. Defant, H. Bellon, J. Z. de Boer, R. H. Stewart, and J. Cotten (1995), Early Tertiary arc volcanics from eastern Panama, in *Geologic and Tectonic Development of the Caribbean Plate Boundary in Southern Central America*, edited by P. Mann, pp. 29–34, Geol. Soc. of Am., Boulder, Colo.

McElhinny, M. W. (1964), Statistical significance of the fold test in paleomagnetism, *Geophys. J. R. Astron. Soc.*, *8*, 338–340, doi:10.1111/j.1365-246X.1964.tb06300.x.

McFadden, P. L., and A. B. Reid (1982), Analysis of paleomagnetic inclination data, *Geophys. J. R. Astron. Soc.*, *69*, 307–319, doi:10.1111/j.1365-246X.1982.tb04950.x.

Molnar, P., and L. R. Sykes (1969), Tectonics of the Caribbean and Middle America regions from focal mechanisms and seismicity, *Geol. Soc. Am. Bull.*, *80*(9), 1639–1684, doi:10.1130/0016-7606(1969)80[1639:TOTCAM]2.0.CO;2.

Montes, C., R. D. Hatcher, and P. A. Restrepo-Pace (2005), Tectonic reconstruction of the northern Andean blocks: Oblique convergence and rotations derived from the kinematics of the Piedras-Girardot area, Colombia, *Tectonophysics*, *399*, 221–250, doi:10.1016/j.tecto.2004.12.024.

Montes, C., G. Guzman, A. Bayona German, A. Cardona, V. Valencia, and A. Jaramillo Carlos (2010), Clockwise rotation of the Santa Marta massif and simultaneous Paleogene to Neogene deformation of the Plato-San Jorge and Cesar-Rancheria basins, *J. South Am. Earth Sci.*, *29*, 832–848, doi:10.1016/j.jsames.2009.07.010.

Montes, C., et al. (2012), Evidence for middle Eocene and younger emergence in Central Panama: Implications for Isthmus closure, *Geol. Soc. Am. Bull.*, doi:10.1130/B30528.1, in press.

Moore, G. F., and K. L. Sender (1995), Fracture zone collision along the south Panama margin, in *Geologic and Tectonic Development of the Caribbean Plate Boundary in Southern Central America*, edited by P. Mann, *Spec. Pap. Geol. Soc. Am.*, *295*, 201–212.

Morell, K. D., D. M. Fisher, and T. W. Gardner (2008), Inner forearc response to subduction of the Panama Fracture Zone, southern Central America, *Earth Planet. Sci. Lett.*, *265*(1–2), 82–95, doi:10.1016/j.epsl.2007.09.039.

Pindell, J. L. (1993), Regional synopsis of Gulf of Mexico and Caribbean evolution, paper presented at Research Conference, Gulf Coast Sect., Soc. of Econ. Paleontol., Houston, Tex.

Pindell, J., and J. F. Dewey (1982), Permo-Triassic reconstruction of western Pangea and the evolution of the Gulf of Mexico/Caribbean region, *Tectonics*, *1*(2), 179–211, doi:10.1029/TC001i002p00179.

Pindell, J. L., and L. Kennan (2009), Tectonic evolution of the Gulf of Mexico, Caribbean and northern South America in the mantle reference frame: An update, in *The Origin and Evolution of the Caribbean Plate*, edited by K. H. James, M. A. Lorente, and J. L. Pindell, *Geol. Soc. Spec. Publ.*, *328*, 1–55, doi:10.1144/SP328.1.

Pindell, J., L. Kennan, W. V. Maresch, K.-P. Stanek, G. Draper, and R. Higgs (2005), Plate kinematics and crustal dynamics of circum-Caribbean arc-continent interactions: Tectonic controls on basin development in proto-Caribbean margins, in *Caribbean-South America Plate Interactions*, edited by H. G. A. Lallemant and V. B. Sisson, *Spec. Pap. Geol. Soc. Am.*, *394*, 7–52, doi:10.1130/0-8137-2394-9.7.

Pratt, T. L., M. Holmes, E. S. Schweig, J. Gomberg, and H. A. Cowan (2003), High resolution seismic imaging of faults beneath Limon Bay, northern Panama Canal, Republic of Panama, *Tectonophysics*, *368*(1–4), 211–227, doi:10.1016/S0040-1951(03)00159-8.

Recchi, G., and A. Metti (1975), Lamina 17, in *Atlas Nacional de Panama*, edited by J. C. Molo, p. 17, Inst. Tommy Guardia, Panama City.

Rockwell, T. K., R. A. Bennett, E. Gath, and P. Franceschi (2010a), Unhinging an indenter: A new tectonic model for the internal deformation of Panama, *Tectonics*, *29*, TC4027, doi:10.1029/2009TC002571.

Rockwell, T. K., et al. (2010b), Neotectonics and paleoseismology of the Limón and Pedro Miguel faults in Panamá: Earthquake hazard to the Panamá Canal, *Bull. Seismol. Soc. Am.*, *100*(6), 3097–3129, doi:10.1785/0120090342.

Rooney, T., P. Franceschi, and C. Hall (2011), Water saturated magmas in the Panama Canal region: A precursor to adakite-like magma generation?, *Contrib. Mineral. Petrol.*, *161*, 373–388.

Rubatto, D. (2002), Zircon trace element geochemistry: Distribution coefficients and the link between U-Pb ages and metamorphism, *Chem. Geol.*, *184*, 123–138, doi:10.1016/S0009-2541(01)00355-2.

Sillitoe, R. H., L. Jaramillo, P. E. Damon, M. Shafiqullah, and R. Escovar (1982), Setting, characteristics, and age of the Andean porphyry copper belt in Colombia, *Econ. Geol.*, *77*(8), 1837–1850, doi:10.2113/gsecongeo.77.8.1837.

Silver, E. A., D. L. Reed, J. E. Tagudin, and D. J. Heil (1990), Implications of the north and south Panama thrust belts for the origin of the Panama orocline, *Tectonics*, *9*(2), 261–281, doi:10.1029/TC009i002p00261.

Silver, E. A., J. Galewsky, and K. D. McIntosh (1995), Variation in structure, style, and driving mechanism of adjoining segments of the North Panama deformed belt, *Spec. Pap. Geol. Soc. Am.*, *295*, 225–233.

Speidel, F., S. Faure, M. T. Smith, and G. McArthur (2001), Exploration and discovery at the Petaquilla Copper-Gold concession, Panama, in *New Mines and Discoveries in Mexico and Central America*, *Spec. Publ. Soc. Econ. Geol.*, *8*, 349–362.

Stewart, R. H., J. L. Stewart, and W. P. Woodring (1980), Geologic map of the Panama Canal and vicinity, Republic of Panama, *U.S. Geol. Surv. Prof. Pap.*, *306-F*.

Torsvik, T., J. Briden, and M. Smethrust (2000), Super IAPD 2000—Paleomagnetic software, Geol. Surv. of Norway, Trondheim.

Trenkamp, R., J. N. Kellogg, J. T. Freymueller, and H. P. Mora (2002), Wide plate margin deformation, southern Central America and northwestern South America, CASA GPS observations, *J. South Am. Earth Sci.*, *15*, 157–171, doi:10.1016/S0895-9811(02)00018-4.

United Nations (1972), Reconnaissance geochemical survey of Bocas del Toro, Maje, Pirre and San Blas-Darien, Panama, report, 77 pp., New York.

Valencia, V. A., J. Ruiz, F. Barra, G. Gehrels, M. Ducea, S. M. Titley, and L. Ochoa-Landin (2005), U-Pb single zircon and Re-Os geochronology from La Caridad Porphyry Copper Deposit: Insights for the duration of magmatism and mineralization in the Nacozari District, Sonora, Mexico, *Miner. Deposita*, *40*, 175–191.

Villagomez, D. (2010), Thermochronology, geochronology and geochemistry of the Western and Central cordilleras and Sierra Nevada de Santa Marta, Colombia: The tectonic evolution of NW South America, PhD thesis, 126 pp., Univ. de Genéve, Geneva, Switzerland.

Wadge, G., and K. Burke (1983), Neogene Caribbean Plate rotation and associated Central American tectonic evolution, *Tectonics*, *2*(6), 633–643, doi:10.1029/TC002i006p00633.

Wegner, W., G. Wörner, M. E. Harmon, and B. R. Jicha (2011), Magmatic history and evolution of the Central American land bridge in Panama since the Cretaceous times, *Geol. Soc. Am. Bull.*, *123*(3–4), 703–724, doi:10.1130/B30109.1.

Weil, A., and A. J. Sussman (2004), Classifying curved orogens based on timing relationships between structural development and vertical-axis rotations, in *Orogenic Curvature: Integrating Paleomagnetic and Structural Analyses*, edited by A. J. Sussman and A. Weil, *Spec. Pap. Geol. Soc. Am.*, *383*. 1–15, doi:10.1130/0-8137-2383-3(2004)383[1:CCOBOT]2.0.CO;2.

Westbrook, G. K. (1990), Gravity anomaly map of the Caribbean region, in *The Geology of North America*, edited by G. Dengo and J. E. Case, plate 7, Geol. Soc. of Am., Boulder, Colo.

Westbrook, G. K., N. C. Hardy, and R. P. Heath (1995), Structure and tectonics of the Panama-Nazca Plate boundary, *Spec. Pap. Geol. Soc. Am.*, *295*, 91–109.

Whitmore, F. C., Jr., and R. H. Stewart (1965), Miocene mammals and Central American seaways: Fauna of the Canal Zone indicates separation of Central and South America during most of the Tertiary, *Science*, *148*(3667), 180–185, doi:10.1126/science.148.3667.180.

Wolters, B. (1986), Seismicity and tectonics of southern Central America and adjacent regions with special attention to the surroundings of Panama, *Tectonophysics*, *128*(1–2), 21–46, doi:10.1016/0040-1951(86)90306-9.

Woodring, W. P. (1957), Geology and description of Tertiary mollusks (gastropods; trochidae to Turritellidae). Geology and paleontology of Canal Zone and adjoining parts of Panama, *U.S. Geol. Surv. Prof. Pap.*, *306-A*, 145 pp.

Wörner, G., R. Harmon, G. Hartmann, and K. Simon (2005), Geology and geochemistry of igneous rocks in the Upper Chagres River Basin, in *The Río Chagres, Panama: A Multidisciplinary Profile of a Tropical Watershed*, edited by R. S. Harmon, pp. 65–82, Springer, Dordrecht, Netherlands.

Wörner, G., R. Harmon, and W. Wegner (2009), Geochemical evolution of igneous rock and changing magma sources during the formation and closure of the Central American land bridge of Panama, in *Backbone of the Americas: Shallow Subduction, Plateau Uplift, and Ridge and Terrane Collision*, edited by S. M. Kay, A. Ramos Victor, and W. R. Dickinson, *Mem. Geol. Soc. Am.*, *204*, 183–196, doi:10.1130/2009.1204(08).

Zijderveld, J. D. A. (1967), A.C. demagnetization of rocks: Analysis of results, in *Methods of Paleomagnetism*, edited by D. W. Collison, K. M. Creer, and S. K. Runcorn, pp. 254–286, Elsevier, New York.

G. Bayona, Corporacion Geologica Ares, Calle 44a #53-96, Bogota, Colombia.

D. M. Buchs, Research Division 4: Dynamics of the Ocean Floor, GEOMAR, Helmholtz Centre for Ocean Research Kiel, Wischhofstr. 1-3, D-24148 Kiel, Germany.

A. Cardona, N. Hoyos, C. A. Jaramillo, and D. A. Ramírez, Smithsonian Tropical Research Institute, Box 0843-03092, Balboa, Panama.

C. Montes, Geociencias, Universidad de los Andes, Cra 1#18A-10, Bogotá DC, Colombia. (cmontes@uniandes.edu.co)

S. Morón, Department of Geology, University of Minnesota, 310 Pillsbury Dr. SE, Minneapolis, MN 55455-0231, USA.

C. A. Silva, Department of Geology, Oklahoma State University, Stillwater, OK 74078-3031, USA.

V. Valencia, Department of Earth and Environmental Sciences, Washington State University, Pullman, WA 99164, USA.